Direct Thermoplastic Impregnation of Leno-Woven Fabric

Pietari Shalah

Degree Thesis

Plastics Technology

2018

Pietari Shalah

DEGREE THESIS	
Arcada	
Degree Program:	Plastics Technology
Identification number:	
Author:	Pietari Shalah
Title:	Direct Thermoplastic Impregnation of Leno-Woven Fabric
Supervisor (Arcada):	Rene Herrmann
Commissioned by:	

Abstract:
To bring high-performance fiber-reinforced composite parts into the mainstream, the parts need to be molded in minutes, easily recyclable and utilize continuous fibers. Current processing methods and materials rely on difficult-to-recycle thermoset resins and long-cycle-time reaction based molding unsuitable for growing demand. Only recently have manufacturing requirements of fiber reinforced composite surpassed current manufacturing capabilities spawning new methods and materials suited for high-volume production. A new all-glass leno-woven unidirectional (UD) non-crimp fabric (NCF) promising structural stability and high permeability was used to demonstrate its suitability for thermoplastic compression resin transfer molding (TP-CRTM) which borrows concepts from thermoplastic injection molding. Through permeability measurements and compression molding this preliminary study investigates the practical feasibility of TP-CRTM using all-glass leno-woven UD NCF and introduces and implements a technique for high-contrast UV fluorescence microscopy. It was demonstrated that higher molding pressures during thermoplastic compression molding improved saturation of the leno-woven UD NCF without overly distorting the fabric structure and that basic UV fluorescence methods resulted in high-contrast images for void detection.

Keywords:	Thermoplastic compression resin transfer molding, UV fluorescence microscopy void analysis, Through-plane permeability measurement, Continuous fiber
Number of pages:	89
Language:	English
Date of acceptance:	

CONTENTS

Figures

Tables

Abbreviations

Abbreviation	Explanation
CFRT	Continuous Fiber Reinforced Thermoplastics
CNC	Computer Numerical Control
CRTM	Compression Resin Transfer Molding
DAQ	Data acquisition
DSLR	Digital Single-Lens Reflex
FTA	Forschungsgesellschaft für Textiltechnik
GSM	Grams per Square Meter
IM	Injection Molding
IMRaD	Introduction, Methods, Results, and Discussion
LCM	Liquid Composite Molding
NCF	Non-Crimp Fabric
PA6	Polyamide 6
PAN	Polyacrylonitrile
PP	Polypropylene
RPM	Rounds Per Minute
TP	Thermoplastic
TP-CRTM	Thermoplastic Compression Resin Transfer Molding
UD	Unidirectional
UI	User Interface
USB	Universal Serial Bus
UV	Ultraviolet
UVB	Ultraviolet B
UVC	Ultraviolet C
VDC	Volts Direct Current
Vf	Fiber Volume fraction
VI	Virtual Instrument

FOREWORD

This thesis was made possible by the Institute of Polymer Engineering (IKT) at the University of Applied Sciences and Arts Northwestern Switzerland (FHNW, Brugg/Windisch) who accepted me as an exchange student and intern. My supervisor Julia Studer and the IKT staff were not only supportive regarding the research but their remarkable hospitality made for a completely worry-free stay in Switzerland. The International Office at FHNW should also be recognized for their outstanding efforts in orchestrating the exchange.

Only through the combination of both great patience and promptitude have Arcada; my co-supervisor, Rene Herrmann; and thesis examiner, Mirja Andersson brought this thesis to its finalization.

Close family and friends were persistent with their reminders to complete this work and can finally be relieved of their thesis-babysitting duties, for now.

1 INTRODUCTION

1.1 Motivation

With growing populations and higher standards of living follows the burden of energy demand and increased emissions. The transportation sector plays a large role in greenhouse gas emissions as presented in [1, Figure 1]. Typically, pollutant-emitting vehicles are operational near commercial and residential zones. With direct threats to the environment and health there are clear incentives for increasing efficiencies of vehicle operation and manufacturing.

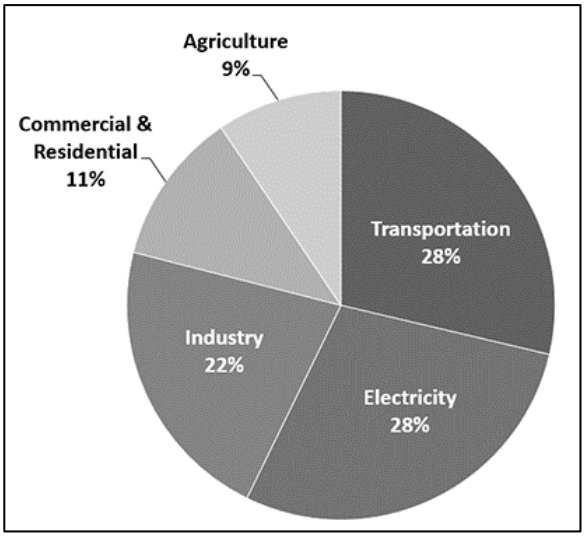

Figure 1 Total U.S. Greenhouse gas emissions by economic sector, 2016. [1]

Vehicle operational losses can be found though the drivetrain, through aerodynamic and rolling drag, and through braking. During city driving, most of the losses can be attributed to braking as shown in the adapted [2, Figure 2]. As all braking involves conversion of energy, there are losses. These losses can be reduced by the reduction of vehicle kinetic energy by lowering vehicle mass.

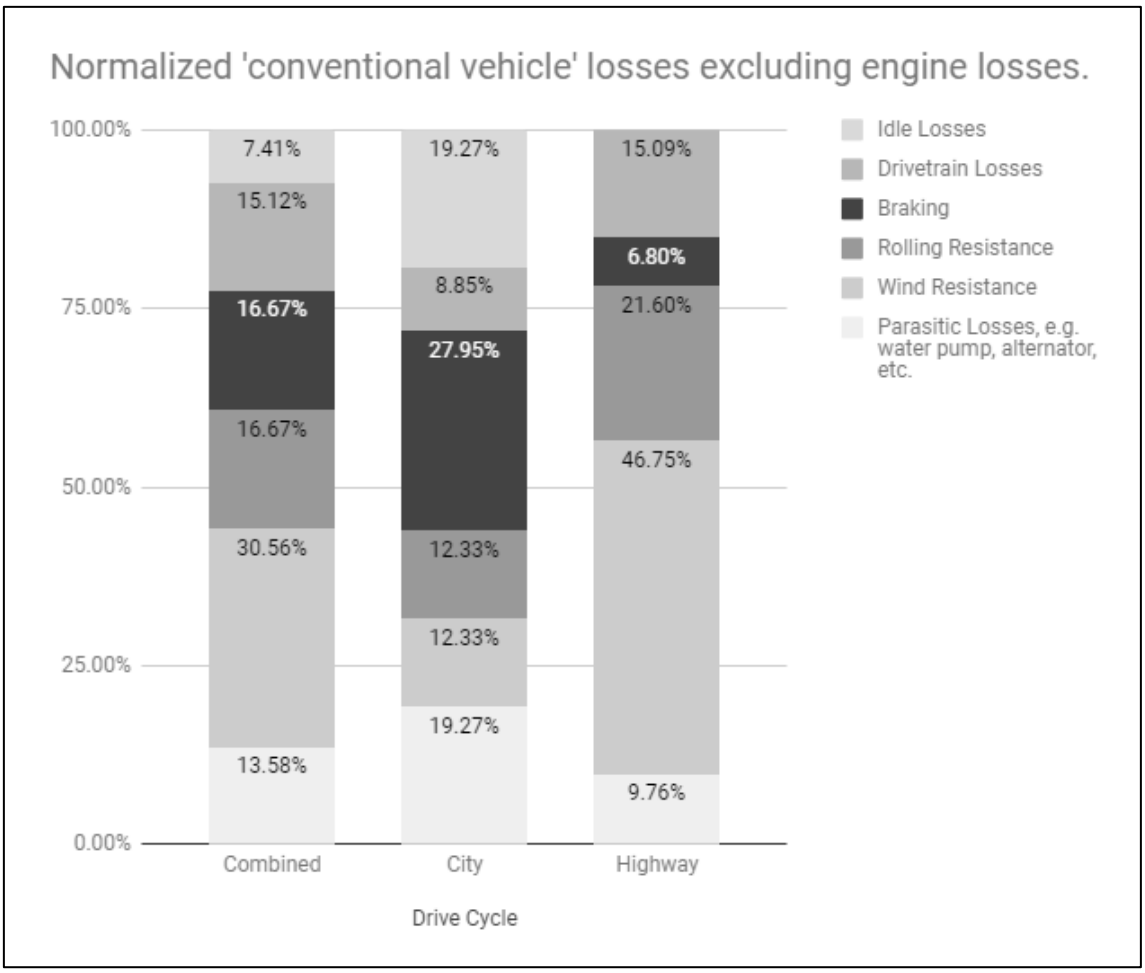

Figure 2 Energy Losses for a Conventional Vehicle for City, Highway, and Combined Driving [2]

In [3] Bjelkengren explains compounding effects of weight reduction. With lighter and smaller parts any supporting structures can now also be lighter and smaller as the load is lessened. This cyclic 'mass de-compounding' will result in weight reductions and down-sizing beyond simply replacing current parts with lighter weight materials. A reduction of 10 g of CO_2 per 100 km has been noted in [4] and [5].

It has been interpreted from [5] that the current methods of light weight composite part production are not cost competitive with traditional methods and materials. Composite part cycle times are too long to keep up with mass manufacturing and the quality of recycled composites are too low to be of any interest.

As the industry is not financially motivated at the moment, there is a gap for academia to fill with answers to stricter emission and materiel waste regulations outlined in [6] and [7]. Compression resin transfer molding thermoplastic (TP) composites aims to provide recyclable composite parts for the transportation industry.

1.2 Background

A lot of the introductory concepts come from two books: *Manufacturing Techniques for Polymer Composites* edited by Suresh G. Advani and Kuand-Ting Hsiao; and *Manufacturing Processes for Advanced Composites* by Flake C. Campbell.

1.2.1 Polymer Composites

Composites are consolidations of two or more materials. Unlike alloying the individual materials remain chemically and physically unaltered. The properties of each component are maintained and the combination of their properties results in a composite with more functional characteristics than either material alone could achieve. [8]

Pristine polymers can be modified by compounding in fibers or particles. The resultant particle/fiber-polymer composite usually exceeds the mechanical properties of the base polymer. Particle type additives are often used to improve toughness and thermal stability while fiber type additives can greatly improve strength and stiffness. [9]

1.2.2 Fibers and Fabrics

Discontinuous fiber reinforcements haven been categorized in [10] as: short (~ 0.5 mm) and long (~ 7 mm). Although highest strength and stiffness improvements are found in continuous fiber reinforcement [9].

In mass manufacturing environments where injection molding is used, fiber filled materials can cause accelerated machine wear during processing; requiring, harder, more expensive tooling. The processing itself also breaks down the majority of longer fibers into much shorter lengths [10], lessening the reinforcing effects of the fibers. This is counterproductive to making light, stiff, and strong parts.

To maximize the benefits of fiber reinforcement, fabrics are produced from continuous fibers. These fabrics can later be infused with a matrix material to form a continuous fiber composite material. Commonly used fiber materials include glass, carbon, and aramid.

1.2.2.1 Fiber Material

This subsection summarizes material from [11].

Glass fibers provide high tensile and impact strength for a low cost. In order of low to high cost: E-glass, S-2 glass, and quartz are common types of glass fiber. Being low cost, E-glass is most common. For mechanically demanding applications S-2 provides about a 40% bump in strength. Quartz glass fiber is an ultra-pure glass used in specialty electrical applications.

Relative to glass, carbon fibers offer much higher stiffness and are less prone to fatigue. Most carbon fibers use polyacrylonitrile (PAN) fibers as a precursor. The PAN fibers are stretched, oxidized, pyrolyzed and finally coated as shown in [11, Figure 3]. The properties of the final carbon fiber are set by the processing variables; tensions, temperatures, and precursor type. Typically, higher heating during carbonization results in higher carbon content and stiffer, stronger, fibers. Carbon fibers made from pitch offer very high stiffness but not as strong as PAN based fibers.

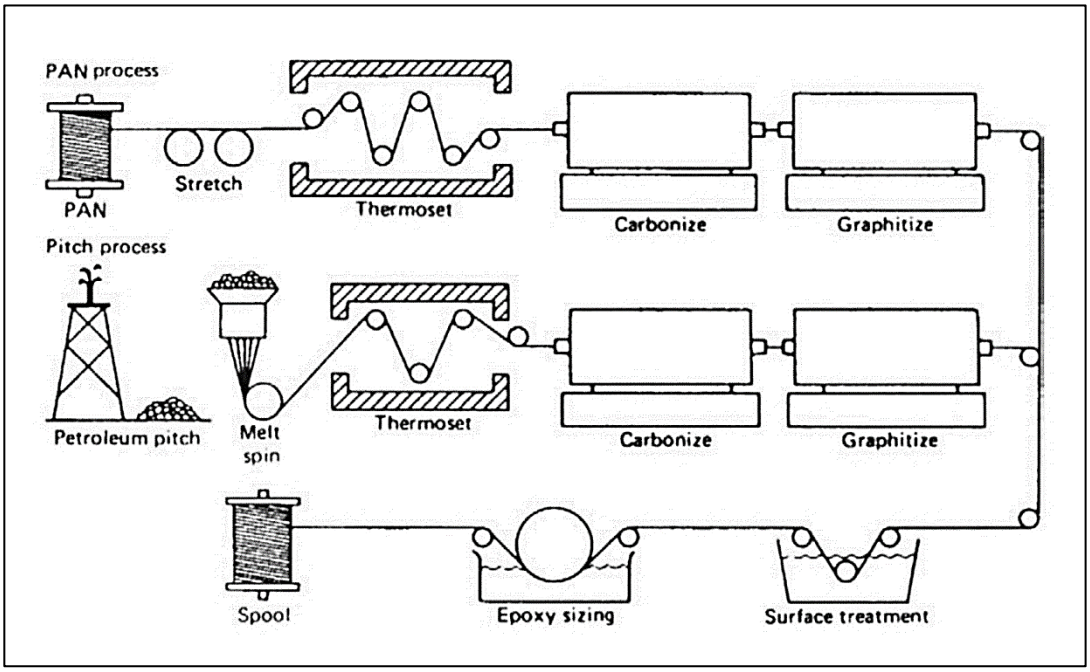

Figure 3 Carbon fiber manufacturing schematic. [11]

Aramids (aromatic polyamide) sit in between carbon and glass fibers in terms of strength and stiffness. Being extremely tough, aramid fibers find uses in ballistic protection applications. Aramids tend to have poor matrix adhesion. With no available adhesion promoting coatings, aramid composites are structurally sound only in longitudinal tension. Carbon and glass fibers both have coatings available which improve matrix adhesion and can handle more off-axis loading.

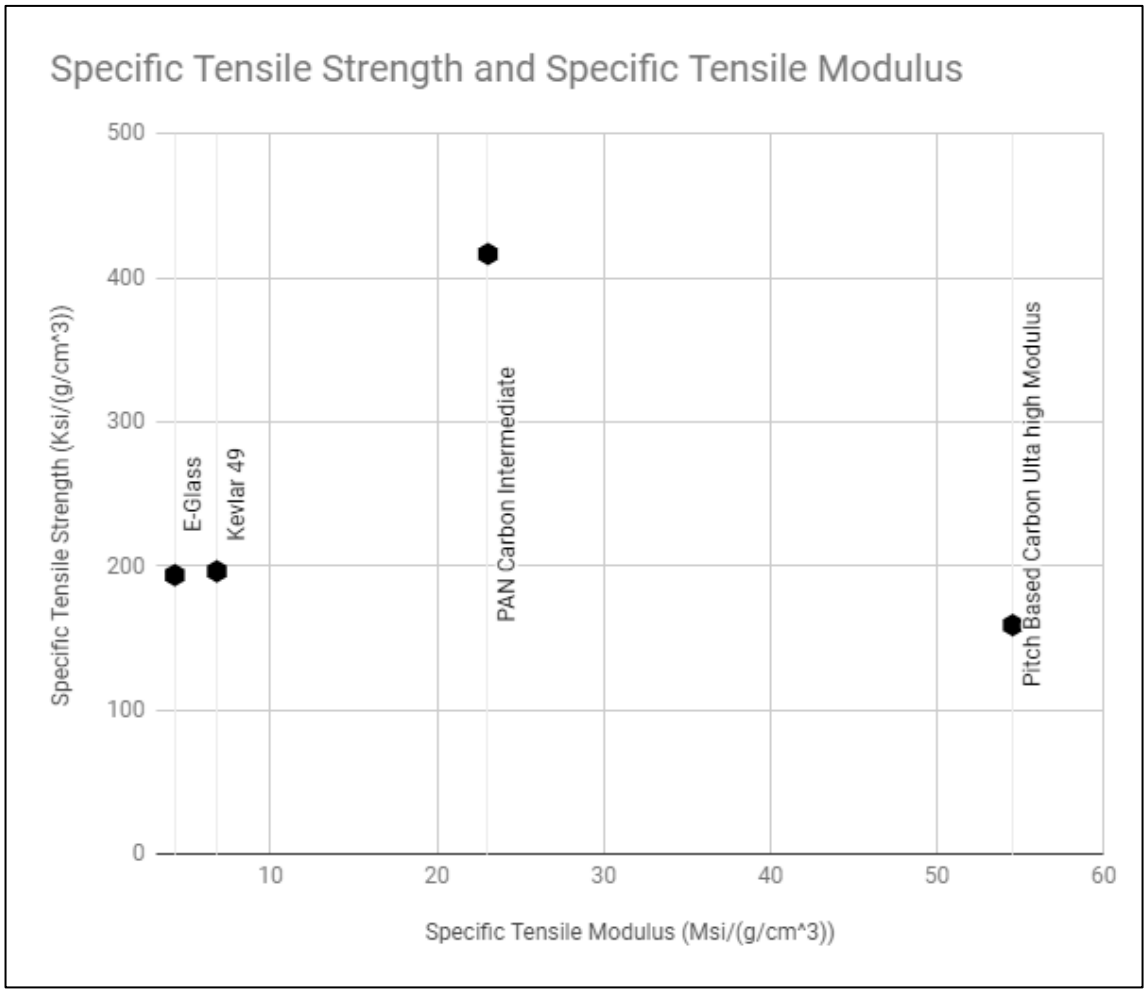

Figure 4 Comparison of different fiber materials. [11]

A comparison of specific strength and specific modulus of select fiber materials is shown in [11, Figure 4].

1.2.2.2 Fabric Architecture

This subsection is also based off [11].

Non-woven fabrics are either chopped or continuous strands (untwisted bundles of fiber) laid down and held together by resin based binders or stitching. The result of varied laying is multi-directional fiber orientation for multi-directional reinforcement. The result of unidirectional (UD) laying results in highly oriented fibers for highly directional reinforcing. UD non-woven fabric is a non-crimp fabric (NCF) as there is no fiber or strand intersections to crimp, bend, the fibers. Drawings of UD and multi-directional non-woven fabrics can be seen in [8, Figure 5] and photographs of the mentioned fabrics are present in [12, Figure 6].

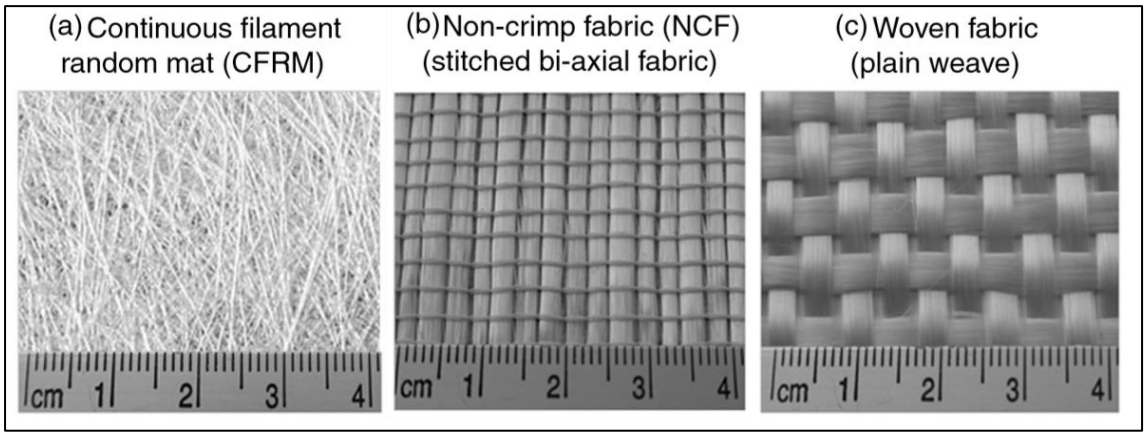

Figure 6 Close-ups of non-woven and woven fabric. [12]

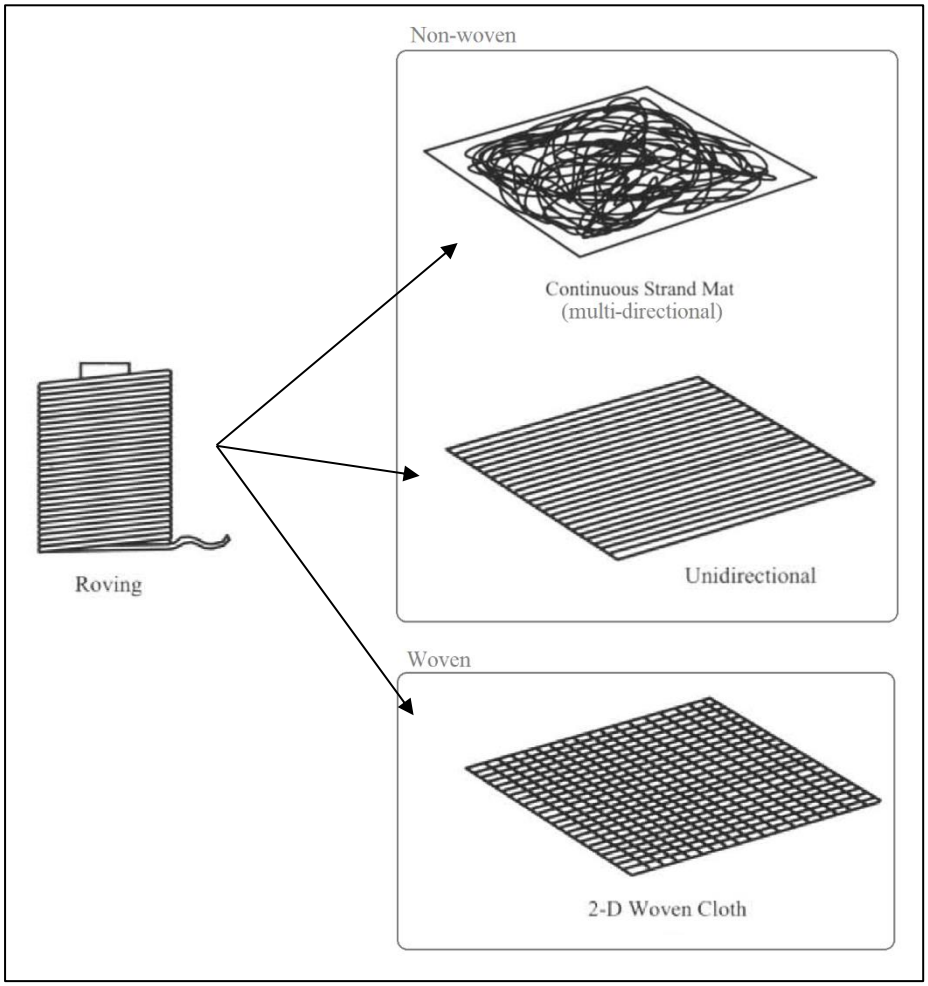

Figure 5 Non-woven and woven fabric examples. [8]

Woven fabrics are often two-dimensional weaves woven on a loom, interlacing two sets of strands at angles to each other usually 0˚ and 90˚ or by rotating the fabric, 45˚ and 45˚.

The size and material of the strands are generally the same. In hybrid weaves the sizes and material makeup of the strands can be altered to achieve different properties and costs.

Different weaves provide different handling properties, drapability, permeability, and waviness (crimping at strand intersections). Use of straighter, less wavy, weaves results in stiffer and stronger composite parts however, highly interlaced fabrics are more stable during handling.

1.2.3 The Matrix

This subsection covers material from [13] and [14].

In fiber reinforced parts the matrix encapsulates all fibers. Loads are transferred to the fibers, absorbing impact and shear loads, protecting the fibers from environmental conditions and preventing microbuckling of the fibers. Continuous fiber reinforced parts overwhelmingly use thermoset resin matrices rather than thermoplastic resins.

1.2.3.1 Thermoset

The low-viscosity nature of thermoset resins has made them de facto matrix materials in continuous fiber polymer composites. Thermoset resins have relatively low viscosities as their monomer molecular weights are low. During curing these monomers begin cross-linking, driven by heat, forming a large, immobile, molecular network. As curing progresses viscosity increases as less monomers are mobile and eventually the liquid resin gels and finally solidifies. These highly cross-linked molecular structures cannot be re-melted and if untoughened resin is used the cured product can show low-strain-to-failure behavior; brittle failure. [13, Figure 7] depicts the transformation from low viscosity monomer to rigid polymer network in a thermoset resin.

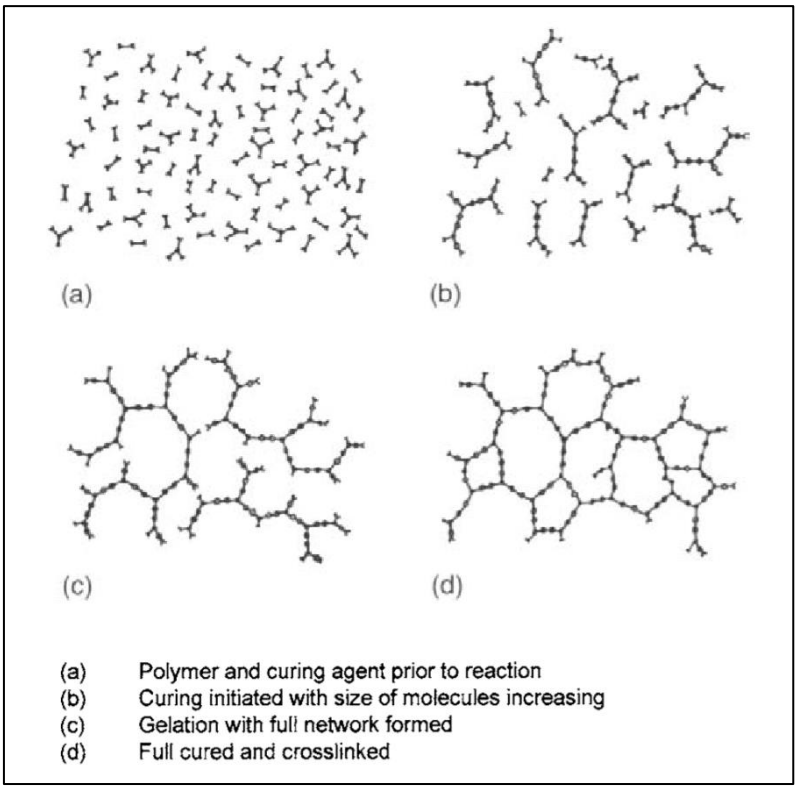

Figure 7 Thermoset crosslinking diagram. [13]

1.2.3.2 Thermoplastic

Thermoplastic resins are high molecular-weight polymers that do not typically cross-link when heated as diagramed in [14, Figure 8], which allows for the remelting and reforming after initial solidification. Comprised of large molecules, thermoplastic processing viscosities are orders of magnitude greater than thermoset viscosities. High viscosity makes for difficult processing, requiring higher pressures and higher temperatures to lower viscosity.

Needing only to be melted, formed and frozen, thermoplastics offer an opportunity for shorter cycle times when compared to fully curing thermoset parts. Being non-reactive, handling, storing, and recycling thermoplastic resins is simpler than thermoset resins.

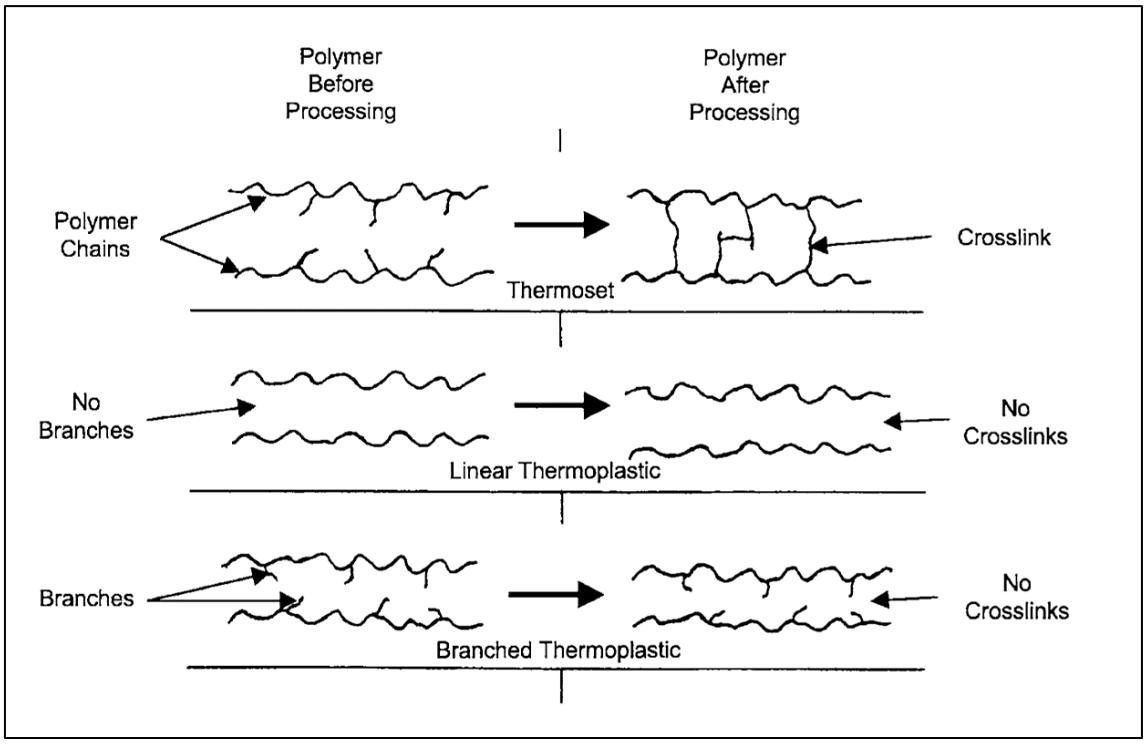

Figure 8 Thermoset crosslinked structure and thermoplastic structure compared. [14]

1.2.4 Processing Methods

It is mentioned in [9] that the ability to fine tune material properties, combined with mass manufacturing methods, hints at why polymer composite parts are replacing many traditionally metal parts. The replacement parts are often lighter, cheaper, corrosion resistant and assembly part count significantly lowered with function integration. In the case of [4, Figure 9] an aluminum wheel was replaced with thermoplastic weighing 30% less.

Figure 9 Injection molded thermoplastic wheel. Material: Long glass fiber reinforced polyamide by BASF. [4]

1.2.4.1 Thermoplastic Injection Molding

As described in [10], injection molding (IM) is a repeatable method suitable for the mass production of plastic parts. An injection molding machine uses a reciprocating screw to convey material into the melt zone and then inject the molten material into the mold. Pressure from the plunging screw forces material into the mold cavity where the molten material solidifies and retains the shape and details of the mold cavity. Once the material is solid enough, the mold is opened, the part is ejected, and the cycle show in [10, Figure 10] repeats.

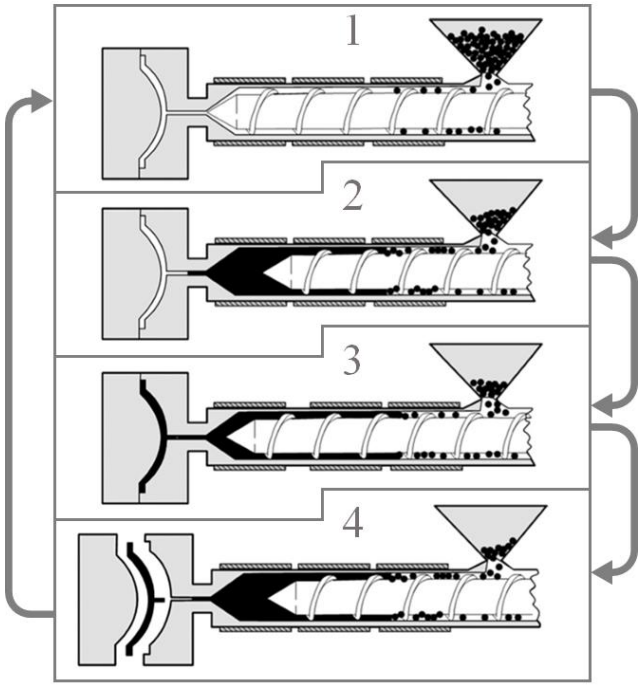

Figure 10 Injection molding cycle diagram. [10]

1.2.4.2 Resin Transfer Molding (RTM)

RTM is classed as a liquid composite molding (LCM) in [15] and suited for medium-volume production where discontinuous fiber composite parts cannot meet mechanical requirements Cycle times are noted at over 15 minutes for RTM in [5].

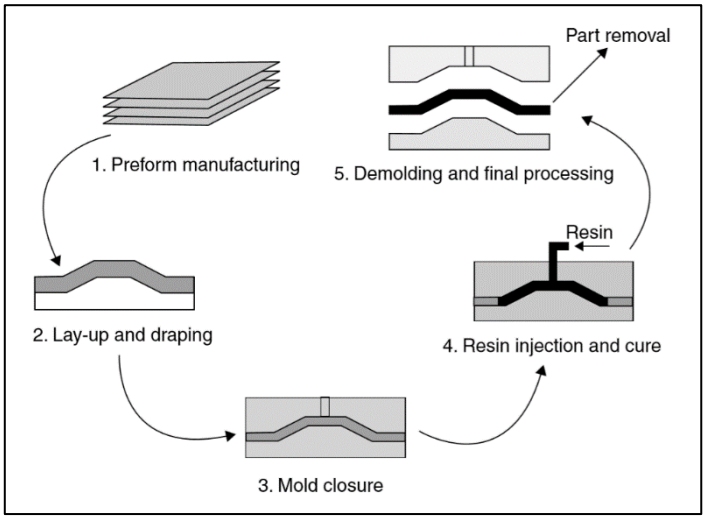

Figure 11 RTM cycle diagram. [15]

[15, Figure 11] is an illustration of the RTM cycle. Dry fabric sub-preforms (plies) are stacked to make up a preform which is draped into the mold cavity. The mold is closed and a low-viscosity thermoset resin is injected into the mold cavity, saturating the fabric preform with resin. Once enough resin has been injected, the injection stops and the resin is allowed to cure.

The reinforcing fabric preform is noted in [12] to be made of fine fibers where there exists micron level inter-fiber spaces which the resin must fill before gelling. To produce void free parts quickly, low-viscosity thermoset resins are primarily used in RTM. [12, Figure 12] shows the direction of impregnation

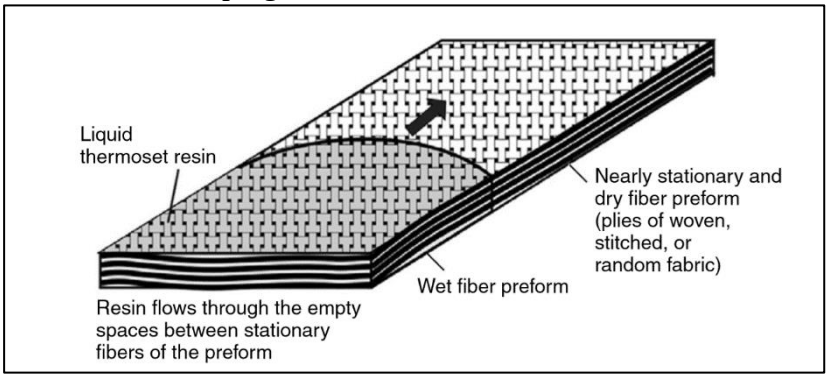

Figure 12 In-plane direction of saturation in RTM. [12]

1.2.4.3 Compression Resin Transfer Molding (CRTM)

CRTM can be considered a modified RTM processes, minimizing impregnation time, for faster cycle times and higher volume production. In an RTM cycle, the mold is fully closed when injected resin flows in-plane through the preform. In-plane distances and low permeability can result in slow saturation times, especially as fiber volume fractions are increased.

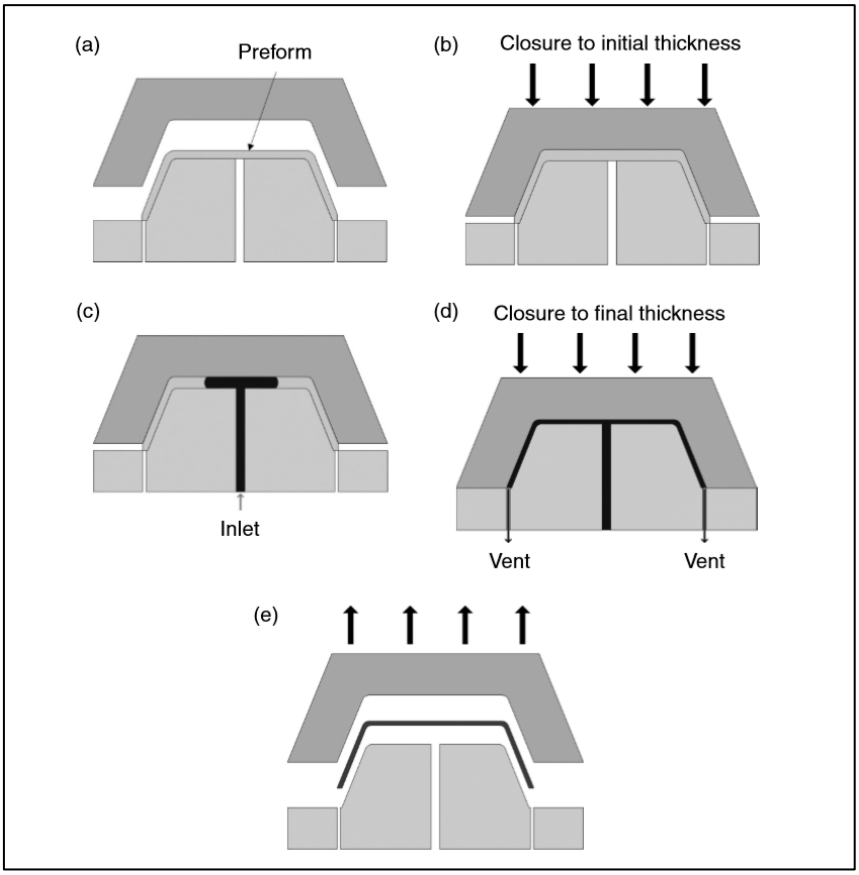

Figure 13 CRTM-1 process overview. (a) Draping preform, (b) partial closure, (c) resin injection, (d) mold closes furthering compressing the resin into the fabric preform, (e) cured part is demolded [16]

In CRTM dry preforms are draped into the mold ready for resin impregnation just as in RTM. However, in CRTM the mold is not fully closed before resin injection. See [16, Figure 13]. With a partially open mold the preform is not fully compressed lowering the fiber volume fraction and increasing permeability. Once the correct resin dose is complete the mold is fully closed forcing resin through the preform. Resin can now permeate in the

through-plane direction which is much shorter than in-plane. CRTM tooling and machinery, needing to deal with greater forces and complexity, will inevitably cost more than RTM tooling.

1.2.5 State of the Art Production Methods

1.2.5.1 Continuous Fiber Reinforced Thermoplastic (CFRT) Thermoforming + Over-molding

To achieve shorter cycle times with CFRT materials, industry has implemented a thermo-stamping method where pre-manufactured CFRT sheets and tapes are formed into parts [17]. The sheets and tapes are pre-consolidated fabric-thermoplastic composites. The stamping process is similar to the current methods of sheet metal stamping [18], with similar waste from edge trimming [5]. The CFRT parts can then be used as inserts for injection over-molding to produce a final thermoplastic IM part with localized continuous fiber reinforcement as shown in [19, Figure 14].

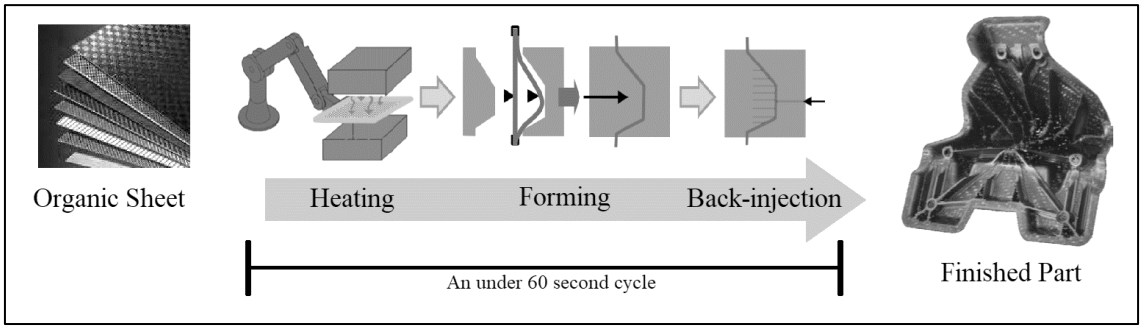

Figure 14 Thermoforming and over-molding of CFRT. [19]

1.2.5.2 MAI Multiskelett

Similar to over-molded thermoformed CFRT inserts, the MAI Multiskelett project aims to combine CFRT truss members with injection molding. The new method attempts to optimize for mass production by combining thermoplastic pultrusion and thermoplastic injection molding, both methods suitable for high-volume production. The concept is show in [20, Figure 15]

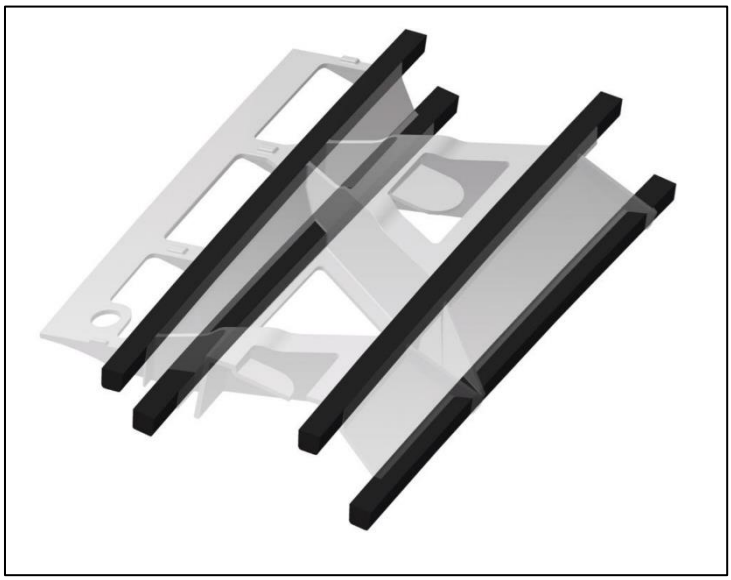

Figure 15 Thermoplastic pultrusion trusses and over-molding concept. [20]

1.2.5.3 Reactive Thermoplastic RTM

An intermediate technology is RTM with the use of thermoplastic monomer. As explained in [21], a very low viscosity liquid is used to infuse a dry fabric preform. In the case of reactive thermoplastic RTM, the liquid is most often a mixture of molten caprolactam monomer, activator and catalyst. As described in [4] and [22] the activator and catalyst are both in separate caprolactam solutions, dosed and mixed right before injection. After the liquid has saturated the preform, it begins to polymerize into a polyamide, a thermoplastic, with the help of a temperature controlled mold. A major drawback to in-mold polymerization reactions are their high sensitivity to humidity [22] and cycle times [5].

1.2.5.4 Recycling

Being multi-component in nature, fiber reinforced composites are inherently difficult to recycle. The goal is to extract the costly fibers intact and undamaged. Any sort of mechanical shredding would result in damaged, discontinuous, fibers. [23]

If the matrix material is a thermoset type, there would be no way of directly re-liquefying the resin. Currently the thermoset resin is baked off (pyrolyzed) leaving the fibers behind. Possibly, in the future, the resin could be dissolved in supercritical water. [24]

There are also efforts going into lining up recycled fibers into discontinuous parallel yarns as a possible method for fiber recovery. This would make for a highly oriented down-cycled material. [25]

For thermoplastic matrices there would be no need to separate the fibers from the matrix and the composite could be reused by remelting the thermoplastic matrix. This property would simplify the down-cycling of the original part to form discontinuous fiber reinforced composite material for either compression molding or injection molding.

1.3 Pervious Works

1.3.1 Injection-Pultrusion of TP Composites

In [26] it was demonstrated consolidation of glass fiber fabric tapes and a low-viscosity polyamide thermoplastic resin. Their photomicrographs show that there are at least two types of flow. Flow in between rovings and flow inside the rovings, between fibers. The resin first races around the rovings and *then* begins penetrating the rovings into inter-fiber space as seen in [26, Figure 16].

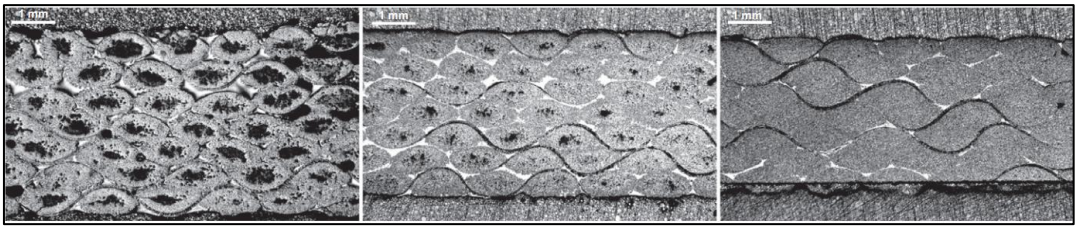

Figure 16 Cross sections of pultruded fabric tapes. Higher processing temperatures to the right. [26]

1.3.2 Permeability Measurement Benchmark

A benchmark exercise [27] documented and compared in-plane permeability experiments in efforts to standardize the procedure. Testing was done assuming homogeneous flow through the fabric making Darcy's law applicable. The report also mentions the importance of sample height as distance is a factor in calculating permeability. While the report was concerned with tool deflection increasing the chamber size and lowering fiber volume fraction, for through-plane measurements there is also the concern of the sample fabric being compressed by the resultant hydraulic pressure of the flowing test fluid. Permeability variations of an order of magnitude were attributed to human error.

1.3.3 TP-CRTM Modeling

A previous paper [28] closely related to this thesis, investigates fabric permeability as a function of fiber volume fraction (Vf) and fiber compaction behavior. The paper presents a model that incorporates a positive correlation between Vf and applied pressure and negative correlation between permeability and Vf. Capillary effects were deemed negligible due to the high pressures and high viscosities involved in TP-CRTM.

1.3.4 Fabric Architecture

During previous experiments at Fachhochschule Nordwestschweiz (FHNW, Switzerland) it was clear that fiber architecture plays a large role. Non-crimp UD type fabrics showed complete bundle deformation during impregnation tests. This deformation filled any inter-bundle voids decreasing permeability. This led to the testing of an all-glass leno-woven UD fabric which aims to provide higher permeability than NCF UD fabrics while maintaining the stability of woven fabrics under high pressures and high temperatures. Often NCF are stitched with thread unsuitable for high temperature molding. The all-glass leno-woven fabric schematic is shown in [37, Figure 17].

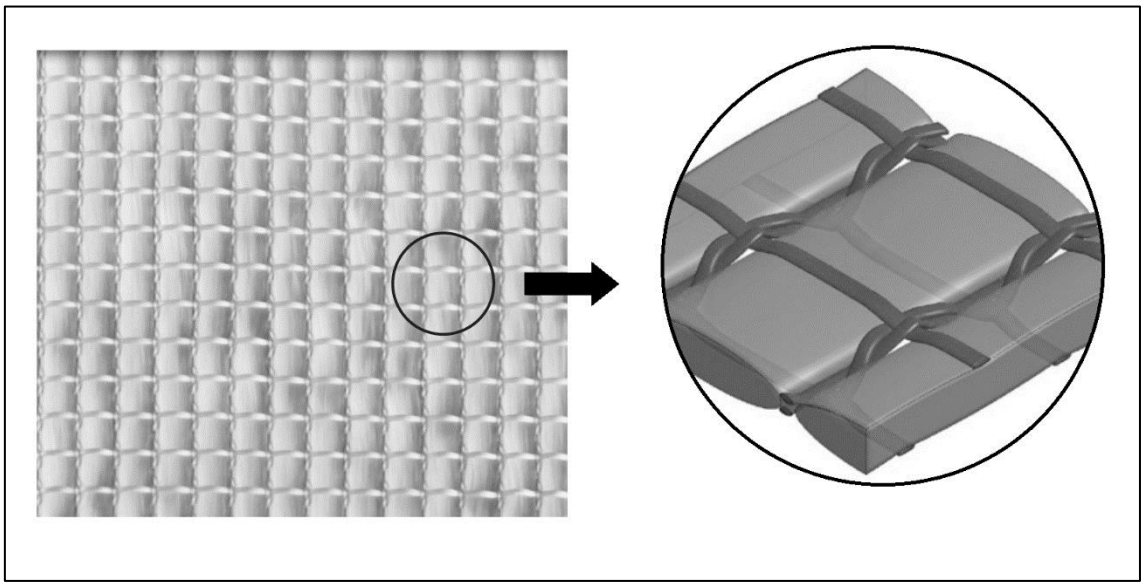

Figure 17 Leno-woven schematic. [37]

1.4 Aim

The aim of this project is to define thermoplastic compression RTM (TP-CRTM) processing parameters that yield fully saturated, void free, composite structures. These processing variables will be compared to fabric permeability properties in attempts to find a relationship between processing variables and fabric permeability properties. In order to quantify saturation of the composite structures, tailored UV fluorescence microscopy methods will be used. The TP-CRTM concept in shown in [29, Figure 18].

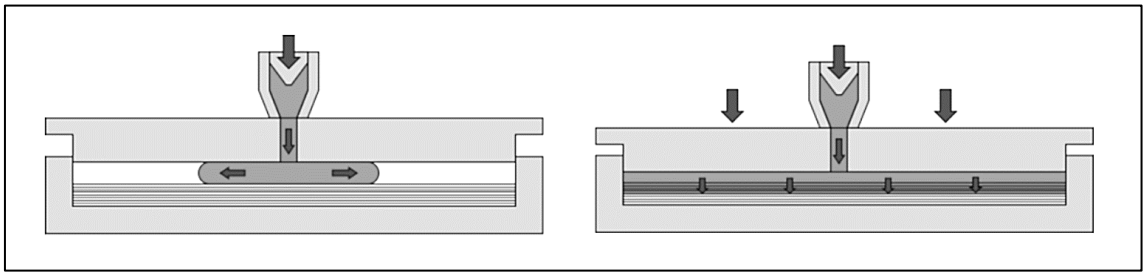

Figure 18 TP-CRTM Concept. Injection molding nozzle into variothermal mold with dry preform insert. First stage: Thermoplastic injection. Second stage: Controlled mold closing. [29]

1.5 Research Questions

1. How does measured fabric permeability relate to manufactured plates?
2. How do TP-CRTM parameters influence impregnation?
3. How can impregnation be quantified?

1.6 Limitations - Scope

The research focus was on thermoplastic impregnation of the fabric and its rovings. Fiber-matrix adhesion was not investigated nor was fiber-matrix wetting. Resulting composite parts were not mechanically tested.

Due to practical and financial limitations impregnation tests took place with a heated and cooled press to simulate injection molding processes and a CRTM mold. A full-on variothermal CRTM mold integrated into an injection molding machine was beyond reach.

An approximation of flow was used when characterizing the fabric permeability. For the use of Darcy's law, the material under-test was assumed to be homogeneous in its permeability.

1.7 Method

Using an apparatus very similar to what would be used to measure hydraulic conductivity (permeability) in soil and Darcy's law, also originating from geology, permeability of fabric stacks was measured.

With the same fabric as in the permeability measurements, plates were molded using a heated press and a thermoplastic resin. The finished plates were then sectioned at areas of interest and samples collected. The samples were then embedded twice, once to fill possible voids with a UV fluorescent resin and a second time to create polished samples ready for UV fluorescence microscopy.

Photomicrographs of the polished samples were taken under UV light. The combination of using a contrasting dye and UV lighting allowed for clear visualization of voids.

1.8 Thesis Structure

This thesis follows the IMRaD framework with a literature review chapter inserted after *Introduction* and before *Methods*.

Following the introduction, a literature review covering the CRTM process, permeability, and leno woven non-crimp fabric (NCF) should provide deeper insight into the experimental process covered in the Methods chapter.

Methods starts off with an introduction to general materials and tools that were used. Later the chapter describes the specific permeability measurement methods, composite plate manufacturing methods, and finally UV fluorescence microscopy methods.

Results are presented in three sections: Fabric permeability analysis, manufactured plate macroscopic analysis, and plate sectional microscopic analysis.

The thesis paper is finalized with a discussion section.

2 LITERATURE REVIEW

2.1 Compression Resin Transfer Molding (CRTM)

2.1.1 Overview

The RTM process stems from the need to produce high performance parts at medium production volumes [30], [31]. Dry fabric preform goes into the mold, the mold is shut, thermoset resin is injected into the mold and the preform is impregnated in the in-plane direction [12]. Durable, rigid, tooling is used to produce repeatable part quality at high injection pressures [15]. Fill times are injection pressure and fiber permeability dependent. Higher injection pressures and higher preform permeability shorten fill times [15]. Mold clamping forces will also increase with increased injection pressure [15].

Demand for larger volumes of higher performance parts have pushed RTM materials and processes to their limits. Short fill times and high fiber volume fractions are incompatible with traditional RTM due to lower fiber permeability and thermoset cure times. CRTM is a slight variation on the RTM cycle but with some interesting outcomes.

2.1.2 The CRTM Process

This subsection summarizes information found in [16].

CRTM introduces mold cavity height control during processing. By varying mold closure, it is possible to control preform compaction, exaggerate through-plane resin flow and increase local resin pressures. Two CRTM scenarios are presented in [16], classed as CRTM-1 and CRTM-2 as shown in [16, Figure 19]. In the CRTM-1 process the mold only partially compacts the preform before injection, keeping the fiber volume fraction low and preform permeability high. In CRTM-2 the mold height is kept high enough to leave an air gap between the mold and preform. This air gap provides extreme permeability minimizing injection times. CRTM-2 is the main candidate for thermoplastic CRTM (TP-CRTM).

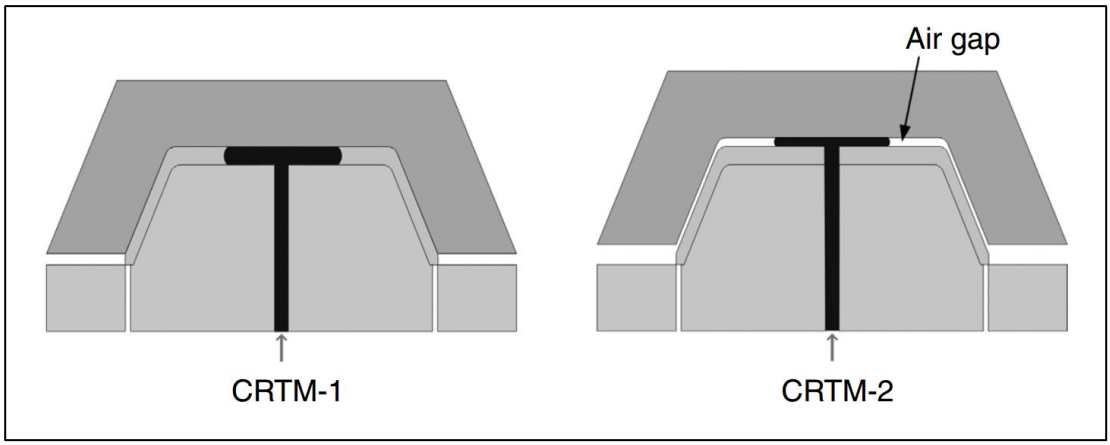

Figure 19 CRTM-1 and CRTM-2 diagrams. [16]

Once the resin is dosed, the mold is closed forcing the resin through the preform. The action of closing the mold imparts a pressure to the whole of the resin area unlike in RTM where the resin-front pressure drops off quickly as it moves away from the injection site. Mold closing itself can be implemented in a few ways. Closing speed and force can be controlled as well as custom speed and force profiles used to maximize impregnation speed. In a general sense, at the early stages of compression where the dry preform is not fully compressed and permeability is high, a high closing speed can be realized with relatively low forces. As the preform compresses and permeability drops, in-mold pressures will build up and resist mold closing requiring either more force or more time to complete the cycle. Adding a seemingly simple variable, mold height control, results in a complex problem of correctly staging injection and mold-closing while optimizing parameters for both.

2.2 Fabric Compaction

2.2.1 Viscoelastic Behavior

Although Bickerton [32] measures behaviors of various fabrics the following review of [32] will focus on the results of the plain weave fabric. Plain weave fabric was tested at higher fiber volume fractions making it more relevant in the context of this thesis.

During CRTM the preform is taken from an uncompressed state to its final compressed state. Bickerton's paper [32] uncovers interesting behavior of dry and saturated fabric when compressed in different modes shown in [32, Figure 20]. Their compaction experiments consisted of using two, solid, flat, parallel plates to compress a dry preform in a controlled manner while logging the resultant forces. Wet experiments were conducted by injecting diluted corn syrup after full compaction to simulate RTM and during compaction to simulate CRTM-1.

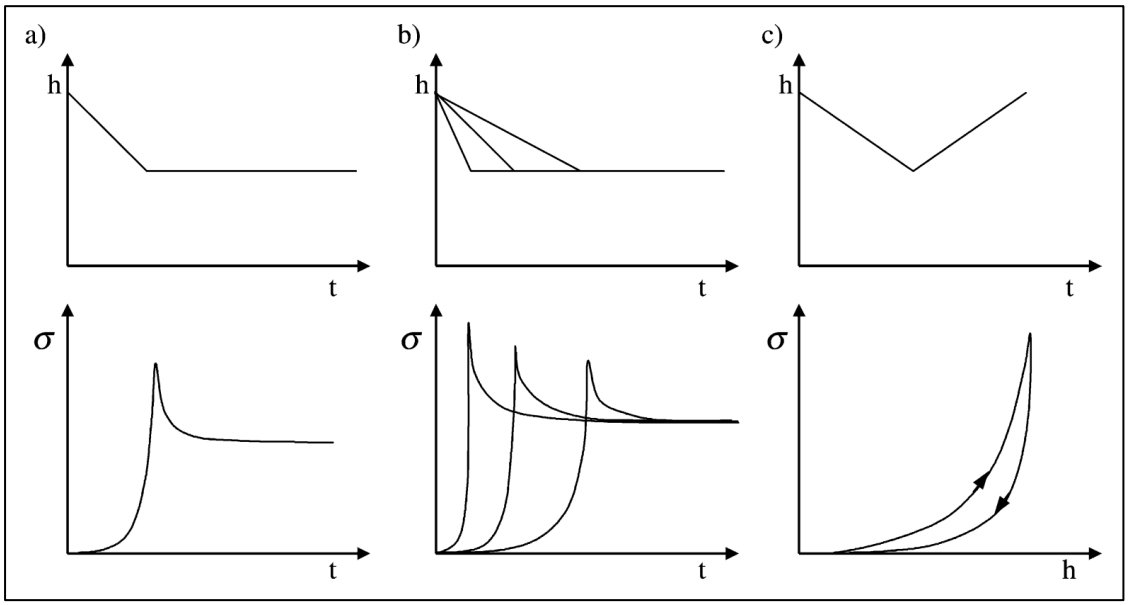

Figure 20 Fabric viscoelastic behavior. h is compaction height and the resulting compressive stresses are shown below. a) Stress relaxation, b) rate dependent behavior, c) fabric hysteresis (x-axis is compaction height). [32]

The general behavior of the dry fabric is described as viscoelastic. Once the compaction motion ends the load quickly drops to a lower level as the fabric relaxes. Peak compression forces and final fiber volume fractions showed positive correlation. Higher fiber volume fractions showed greater relaxation. The injection of the diluted corn syrup also resulted in greater relaxation, it is mentioned that this may be caused by lubricating effects of the fluid.

Higher compression speeds resulted in greater relaxation percentages and during the 52.5% fiber volume fraction test, higher compression speeds also resulted in absolute lower final stresses. It was only during the 62.5% fiber volume fraction test where peak stress was much higher with a fast closing action. The graphs in [32, Figure 21] show very slow closure speeds resulting in high forces, possibly due to nesting effects of the woven fabric.

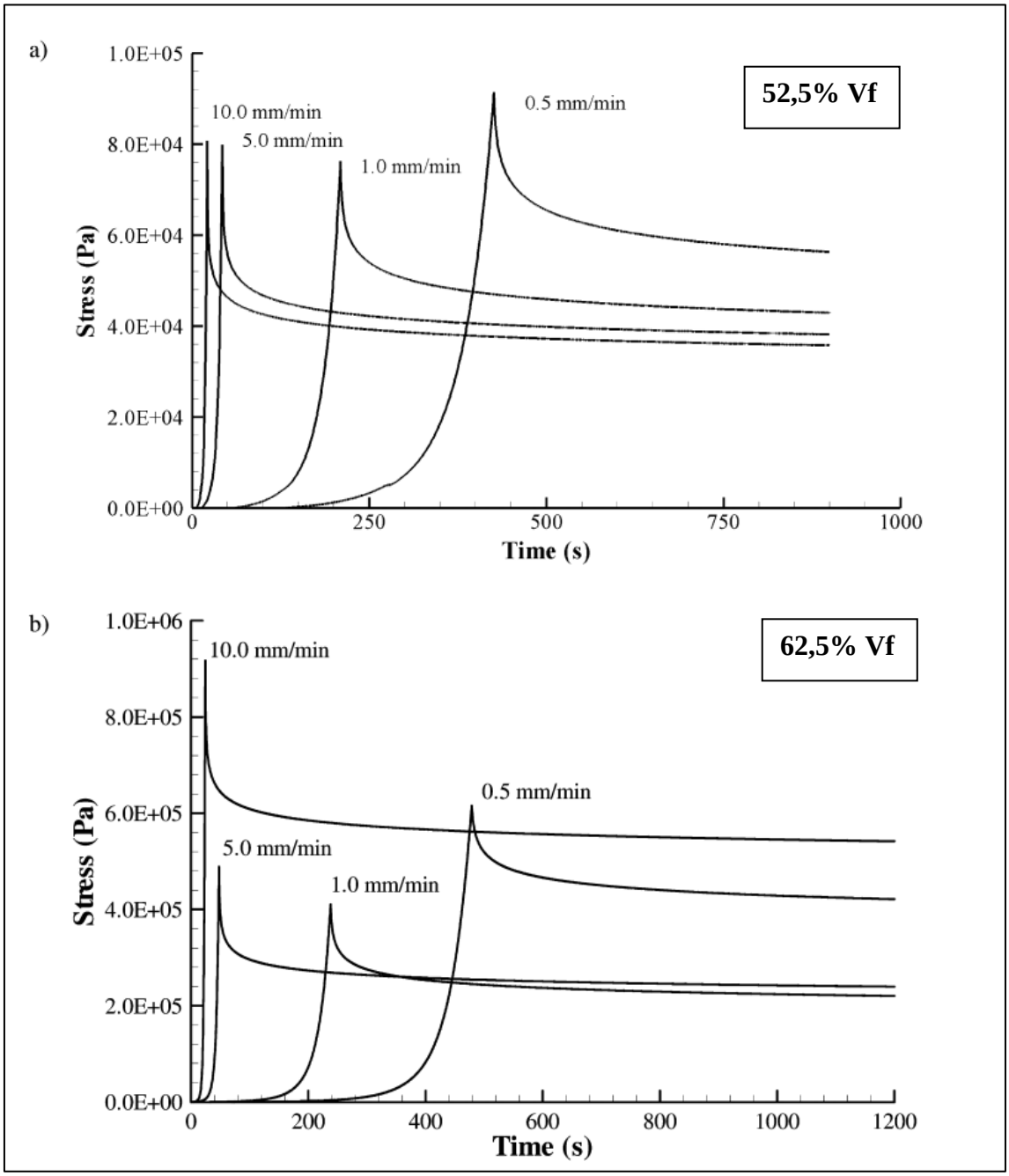

Figure 21 Plain weave fabric compression speed tests. a) 52,5 Vf and b) 62,5 Vf [32]

Closure speeds were slow at 0.5-10.0 mm/min during the testing. Since there was no clear trend of higher stress levels at higher speeds, it is difficult to conclude what kind of stresses will exist during much faster compaction. Higher closing speeds seem to result in more elastic behavior.

2.2.2 Terzaghi's Law

Terzaghi proposed that stresses in water-saturated porous soil are shared between the fluid and the porous solid media [33]. In a CRTM process where a saturation gradient exists there also exists a gradient in stress sharing as shown in [29, Figure 22]. In the absence of either the fluid or solid component the remaining component bears the full load. As saturation progresses the load is proportionally shared between the fluid and the porous solid.

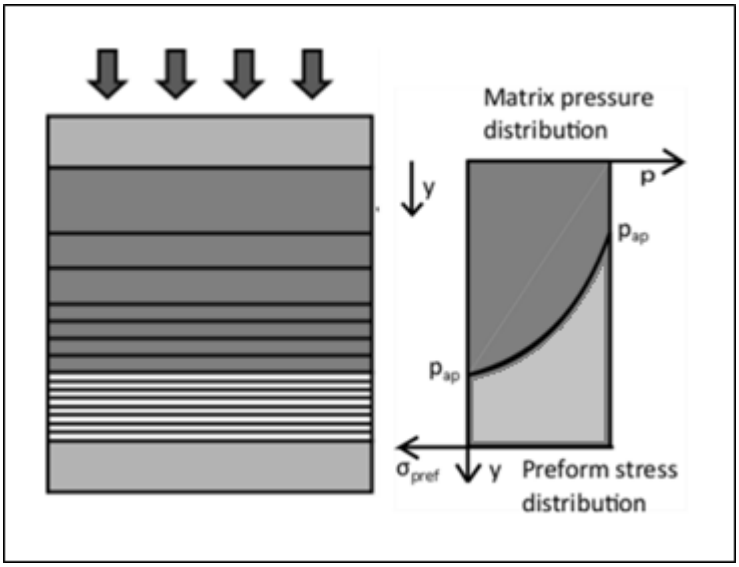

Figure 22 Pressure, stress and compaction gradient in compression molding. [29]

In a fabric-resin system the stresses cause the fabric to compress in a way that is characterized by the fabric's compaction curve [34]. As the fabric continues to saturate along the flow front the resin shares part of the overall stress and the fabric begins to relax at its new, lower, stress level. Once the fabric is fully saturated the relaxation behavior of the fabric will cause it to evenly fill the height and the load is evenly shared by any hydrostatic pressure of the resin and the compacted fabric. A spring analogy is often used to explain the loading relationship, see [35, Figure 23] which is adapted from [35] and [34].

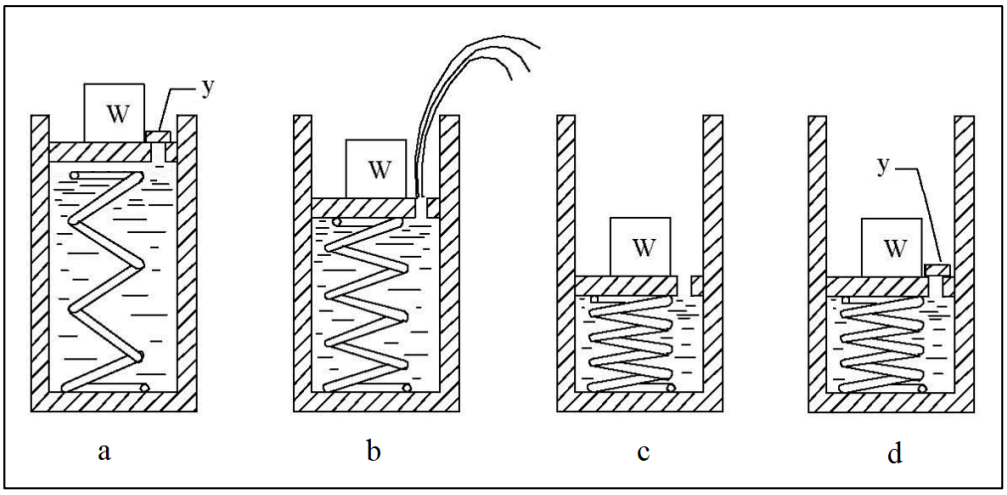

Figure 23 The Terzaghi Spring Analogy. At 'a' piston is hydrostatically locked (y) and only fluid supports the load. At 'b' both fluid and spring support the load. At 'c' only the spring supports the load. At 'd' both fluid and spring support the load. [35]

2.2.3 Darcy's Law

Darcy's Law describes fluid flow through a fully saturated porous solid under steady state. A level of permeability is derived from the relation of flow rate through the porous solid and the pressure required to produce that flow. [12]

Darcy's formula as seen [36, eq.(1)] is used in this thesis for calculating permeability.

$$\kappa = \frac{-Q\mu L}{A(pb - pa)} \tag{1}$$

Fluid volume flow is $\boldsymbol{Q}$ in $m^3 s^{-1}$. Fluid viscosity is $\boldsymbol{\mu}$ in $Pa \cdot s$. The length of the porous solid is $\boldsymbol{L}$ in m. The cross-sectional area of the porous solid is $\boldsymbol{A}$ in m^2. The pressure drop is difference between outlet and inlet pressure ($\boldsymbol{pb} - \boldsymbol{pa}$) in Pa. Permeability is $\boldsymbol{\kappa}$ in m^2.

3 METHOD

This section will cover methods and materials for three procedures: *Permeability testing*, *composite plate manufacturing* and *UV fluorescence microscopy*. Permeability testing was carried out to investigate how different volume fractions and pressure gradients affect permeability. Thermoplastic composite plates were manufactured and inspected in order to explore different processing parameters and their influences on the final part. UV fluorescent microscopy was used to detect void content of the molded plates.

3.1 Materials

The materials list has been divided to represent the three main procedures plus the shared procedure of fabric cutting. FTA is an abbreviation for Forschungsgesellschaft für Textiltechnik Albstadt, the supplier for the fabric tested.

3.1.1 Fabric Cutting

- CNC fabric cutter [Manufacturer: Zund]
- 10-sided rotary blade [Manufacturer: Zund]
- Leno-Woven NCF 1280 GSM, Fiberglass [Manufacturer: FTA]
- Leno-Woven NCF 540 GSM, Fiberglass [Manufacturer: FTA]
- Vacuum cover film
- Backing paper

3.1.2 Permeability Testing

3.1.2.1 Equipment

- Compression and pumping apparatus
- National Instruments USB DAQ 6000 series
- Differential Pressure Meter [Model: testo 512]
- Piezoresistive Absolute Pressure Sensors [Manufacturer: Kistler]
- Piezoresistive Amplifiers [Manufacturer: Kistler]
- Digital scale with serial output [Manufacturer: KERN Model: PCB]
- Serial to USB interface

3.1.2.2 Consumables

- Silicone Oil, 47 V 100; 0.1 $Pa \cdot s$; 965 kg/m^3 [Manufacturer: Bluestar Silicones]
- Pre-cut plies

3.1.3 Thermoplastic Plate Manufacturing

3.1.3.1 Equipment

- Temperature controlled hydraulic Press
- CRTM steel mold
- Dead-blow hammers
- Soft prying tools
- Polymer blasting cabinet
- Digital weighing scale

3.1.3.2 Consumables

- Pre-cut plies
- Fiber-grade Polypropylene (PP) [Borflow™ HL512]
- Specialty low-viscosity Polyamide 6 (PA6)
- High-temp release agent [Loctite® Frekote®]
- Viton® O-rings

3.1.4 UV Fluorescence Microscopy Sample Preparation

3.1.4.1 Equipment

- Polishing/ lapping machine [Manufacturer: STRUERS, Model: Tegrapol]
- Digital optical microscope [Manufacturer: Keyence]
- Modern digital camera with macro lens [Manufacturer: Nikon]
- Hacksaw
- Paper guillotine
- Specimen leveling press

3.1.4.2 Consumables

- Rhodamine B doped clear epoxy resin
- Two-part polyurethane CEM 9000 casting resin [Manufacturer: Cloeren Technology GmbH]
- Lapping film
- Polishing solution
- Modeling clay
- Microscope slides

3.2 Fabric Preform Preparation

To produce hundreds of plies for both permeability and molding experiments machine-cut samples were used. Manual cutting is too slow, too inconsistent and unsuitable for delicate, dry, fabric. If in-house machine-cutting isn't an option, outsourcing is recommended. As setup and cleanup times are longer than cut times it is advised to maximize sample count per machine cycle by utilizing the full work-area of the machine. It is also advised to consider unsupported rovings at the edges of the cut which can separate completely, especially with UD fabrics.

Leno-woven UD fabric was chosen for its ability to maintain inter-roving separation during processing. Higher permeability from separated rovings should assist in successfully impregnating the fabric.

All manipulation was by gloved hand.

3.2.1 Shapes Used

The rounded rectangle shape was used for thermoplastic compression molding and the circular shape was used for permeability measurements, see [Figure 24]. These shapes match the shapes of their respective test-cavities.

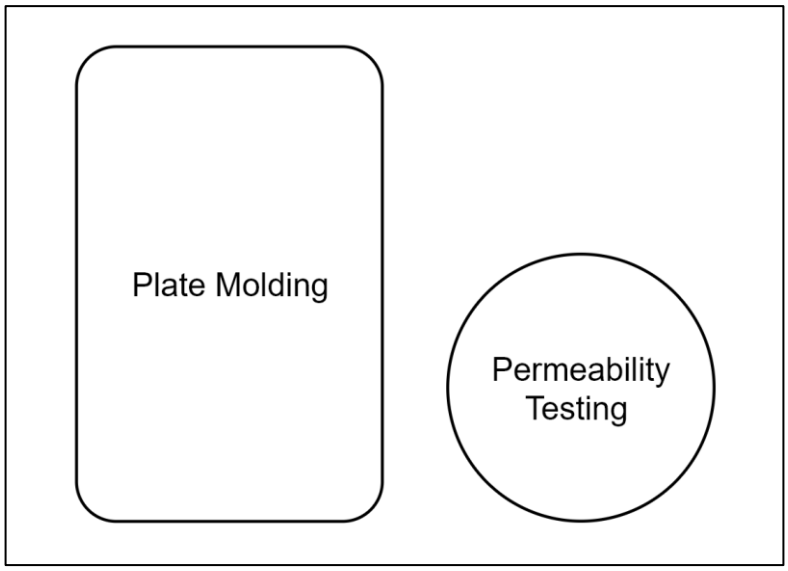

Figure 24 Ply shapes used, not to scale. [Author]

3.2.2 Cutting Procedure

3.2.2.1 Fabric Placement

First, backing paper was unrolled onto the cutter bed. UD leno-woven fabric was then unrolled onto the paper. The fabric was manually manipulated and roughly oriented to an axis of the Cartesian machine. The fabric was then covered with a thin plastic vacuum-film that covered the fabric and extended out in all directions covering the bed of the machine. This film was then ironed out by hand and one whole edge was firmly attached with sticky tape to the machine bed. The film was ironed out once more and the work-holding vacuum bed was turned on.

With the vacuum on, the stack was firmly pressed onto the bed. The tool head's laser pointer was used to mark a point grid onto the film. The marking was done manually by permanent marker. After marking a coarse grid over the film, the vacuum was shut off. The film was gently lifted from the non-taped side and the fabric was manually adjusted under the film. The film was placed back down, vacuum turned on and alignment to the hand-marked grid inspected. This cycle of lifting the film and adjusting the fabric was repeated a couple of times to achieve acceptable alignment. The machine bed and stack of plastic fabric and paper is illustrated in [38, Figure 25].

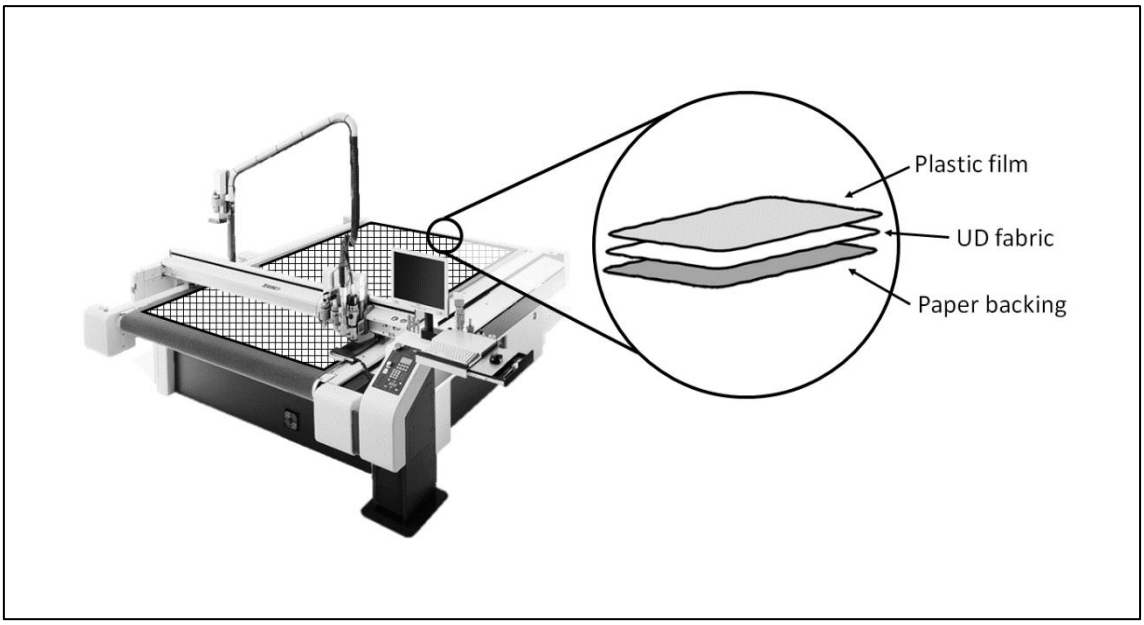

Figure 25 CNC fabric cutter setup. [38]

3.2.2.2 Ply Cutting

A 10-sided (decagon) rotary knife of about 40 mm in diameter was used for all cutting operations. See [Figure 26].

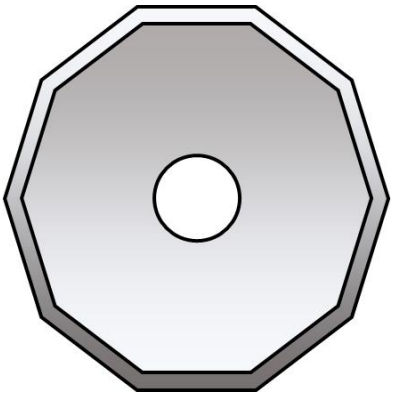

Figure 26 Decagonal rotary blade illustration. [Author]

Once the fabric was aligned, one of the two shapes was chosen to be cut. A sanity check was run including a test cut to verify a successful cut and adjust depth of cut. With everything set the shape is programmed to be cut multiple times throughout the whole fabric area as shown in [Figure 27]. A single shape per sheet was used for easier nesting and manual extraction from the bulk fabric.

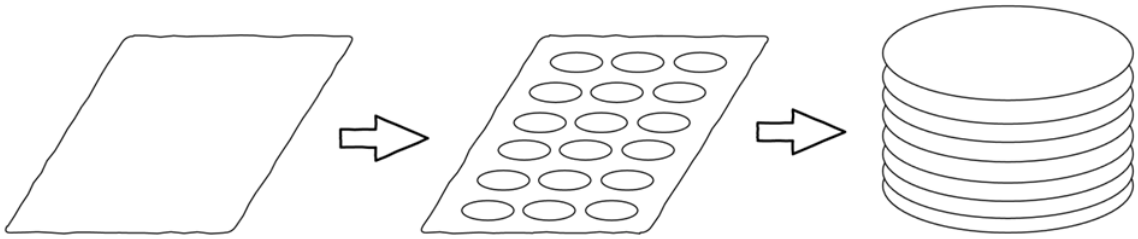

Figure 27 From fabric to preform. [Author]

3.2.3 Storage and Handling

Due to the nature of the FTA leno-woven NCF and cut orientation, edges of the cut plies tended to lose rovings during handling, see [Figure 28]. A light touch and a supportive container was used. For round samples a deep cup worked well and for rectangular samples a box with extra padding was used.

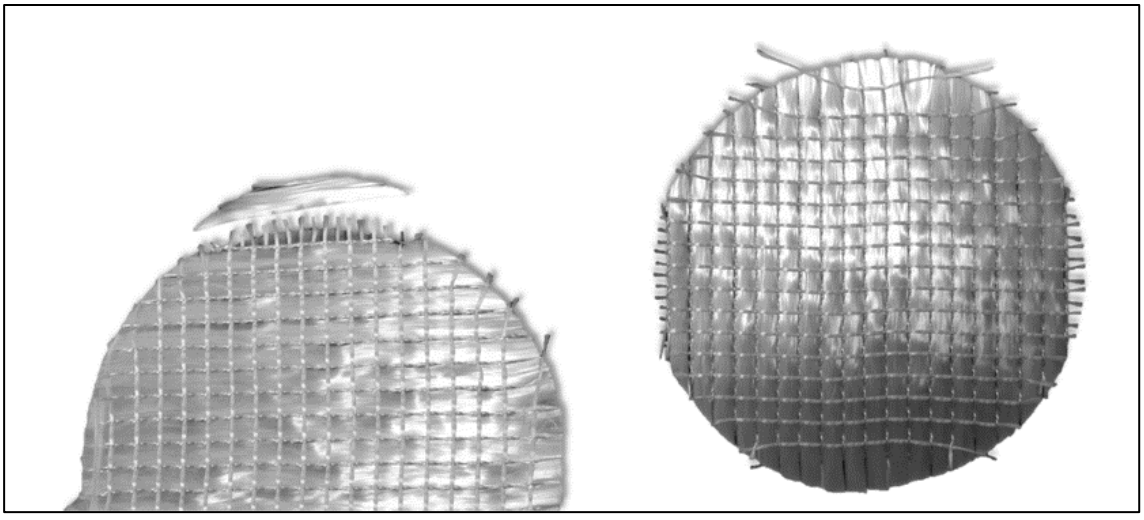

Figure 28 Lost rovings from plies. [Author]

3.3 Fabric Permeability Testing

This section will cover the testing apparatus, testing procedure, data acquisition (DAQ) and data analysis methods used to characterize fabric permeability.

3.3.1 Process Detail

3.3.1.1 Testing Apparatus

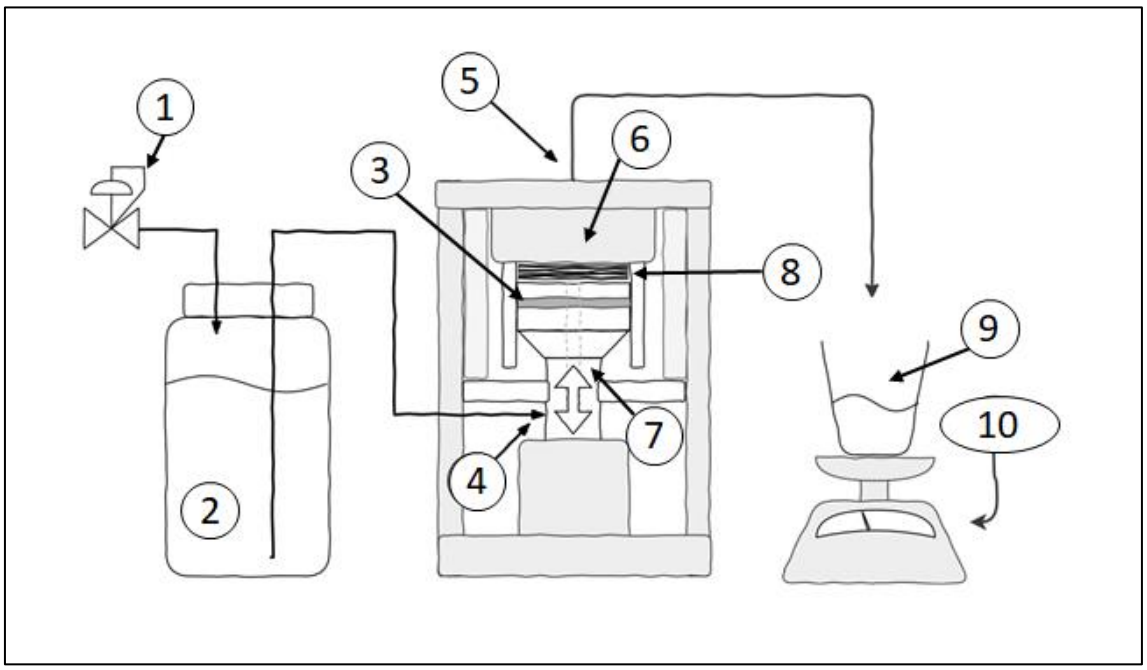

Figure 29 Testing apparatus schematic. 1) Air pressure regulator. 2) Oil tank. 3) Hydraulic seal. 4) Inlet pressure sensor. 5) Outlet pressure sensor. 6) Locking top lid. 7) Hydraulically actuated compression piston. 8) Fabric stack specimen. 9) Oil collection and weighing cup. 10) Digital weighing scale. [Author]

The setup, [Figure 29], consisted of an oil tank which was pressurized with air through a manually operated pressure regulator. The oil was plumbed from the tank, through the compression piston and into the test chamber through a fluid diffusing nozzle which doubled as the piston head. The nozzle consisted of a few mm tall fluid maze. An aluminum honeycomb sandwich material of about 15 mm thick was placed onto the maze. The honeycomb was used to isolate the fabric stack from the diffusion maze. The honeycomb was acting as the interface between the piston head and fabric.

The compression piston was hydraulically actuated and the piston compressed the test fabric stack to a height set by steel spacers. Gap height was set by using specifically sized spacers, 20 mm. During piston actuation the fabric was pressed against the locking top lid of the test chamber which also featured an aluminum honeycomb followed by a fluid

diffusion maze. The oil flowed out the lid, through a hose, and was collected into a cup which was located on a digital scale.

There were piezoresistive pressure sensors located at the inlet and outlet. The inlet being the fabric-compressing piston and the outlet being the locking lid. Data from the two sensors and digital scale was logged on to a personal computer. Details can be found in the data acquisition section bellow.

3.3.1.2 Sample Preparation

As described above, the plies were cut out from a larger sheet. The plies are round and were stacked manually into the test chamber one at a time. The edges of the cutouts were prone to losing a roving or two. If the lost roving was large enough the sample was scrapped and a more intact sample was used. The samples were handled carefully and could be placed by tweezer if the operators hand didn't fit inside the chamber.

A predetermined number of plies were stacked on top of each other. The plies were visually placed in the same orientation.

$$n = \frac{Vf\ pf\ h}{Aw} \tag{2}$$

Equation [eq. 2] was used to calculate ply count. Desired fiber volume fraction is $\boldsymbol{V_f}$, and set between 0 and 1. Fiber material density is $\boldsymbol{p_f}$ in kg/m^3. Cavity height is $\boldsymbol{h}$ in m. Fabric areal weight is $\boldsymbol{A_w}$ in kg/m^2. Ply count is $\boldsymbol{n}$ and it was rounded to the nearest whole number. The whole number was then used to calculate the actual fiber volume fraction and compared to desired fiber volume fraction.

3.3.1.3 Process Variables

Two main variables were varied; fluid inlet pressure and fiber volume fraction. The fluid pressure was varied by the means of a manually operated pneumatic pressure regulator which fed air into the sealed oil tank via air hose. Fiber volume fraction was varied by laying up a different number of plies. Pressure was categorized into high and low pressure

corresponding to 1,0 bar and 0,5 bar as indicated on the analog dial on the pressure regulator. While pressure was cycled as in [Figure 30] between high and low during the experiments, chamber height and layer count remained fixed per experiment.

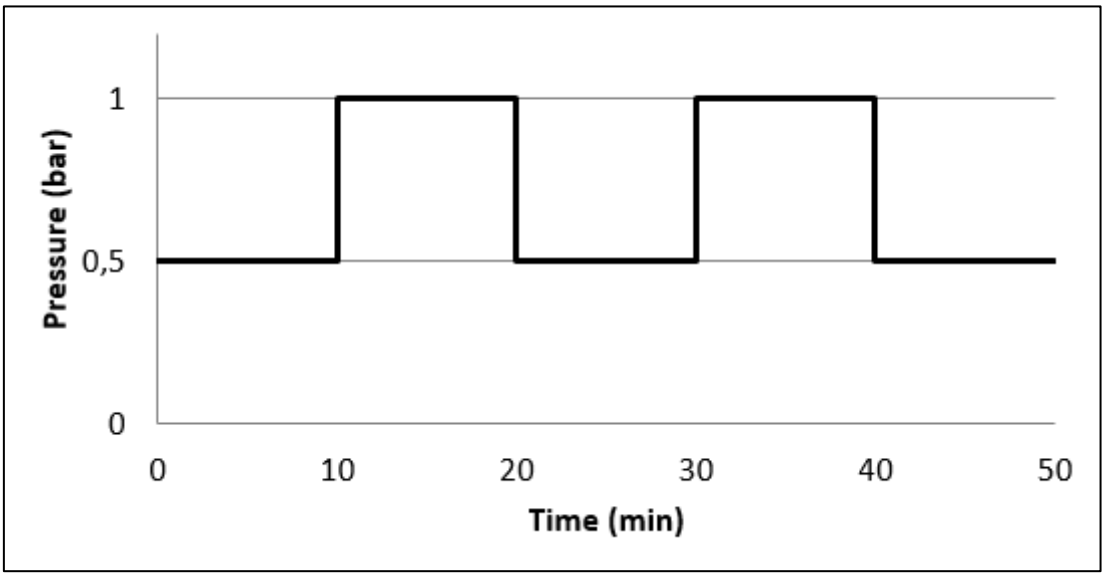

Figure 30 Pressure cycle for permeability measurement. [Author]

The same silicone oil was used and recycled for all experiments. The oil was gravity filtered through a very fine stainless-steel mesh after each use.

3.3.1.4 Process Description

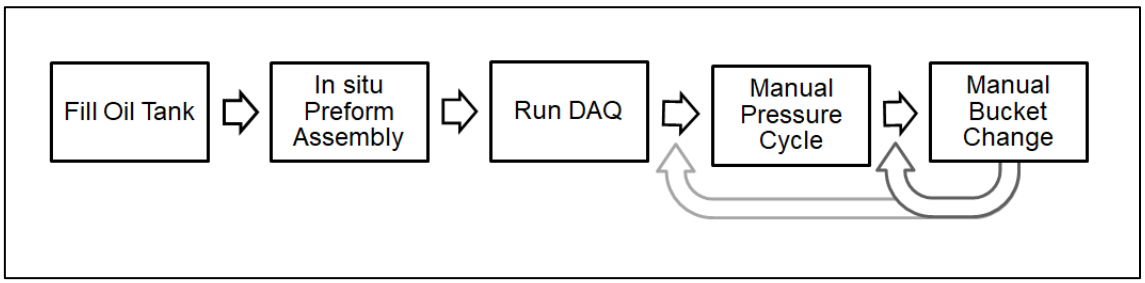

Figure 31 Sequence of operations for permeability measurement. [Author]

First the oil tank was filled with about 2 L of filtered silicone oil. With the hydraulic piston in the lower position the fabric stack was manually assembled by layering individual plies on top of each other, oriented in the same direction. Once all layers were placed and the correct height spacers were in place, the lid was placed on top and locked down.

The dry fabric stack was then compacted to the set height by actuating the hydraulic piston.

With the fiber stack compressed, the oil tank was pressurized through the pneumatic regulator. To promote the release of trapped air in the system, rapid pressurization and depressurization cycles were utilized. Once the system was practically air-free data logging was initiated and a regular cycle of low and high pressure was implemented. Due to a check valve, input pressure would not drop quickly and venting was required when transitioning from the high-pressure state to the low-pressure state. Low to high pressure transitions behaved as expected with predictable settling times. About 10 minutes was spent per low or high-pressure state to collect data, this was typically the interval at which the scale would reach its capacity limit of a few hundred grams and an empty cup would replace the filled cup. Total experiment duration was limited by the starting volume of oil and average flow throughout the experiment. Once all the oil was pumped through, data logging was terminated and the whole setup was depressurized and cleaned. The data log was copied and stored in a descriptively named directory along with any notes related to the test.

3.3.2 Data Acquisition

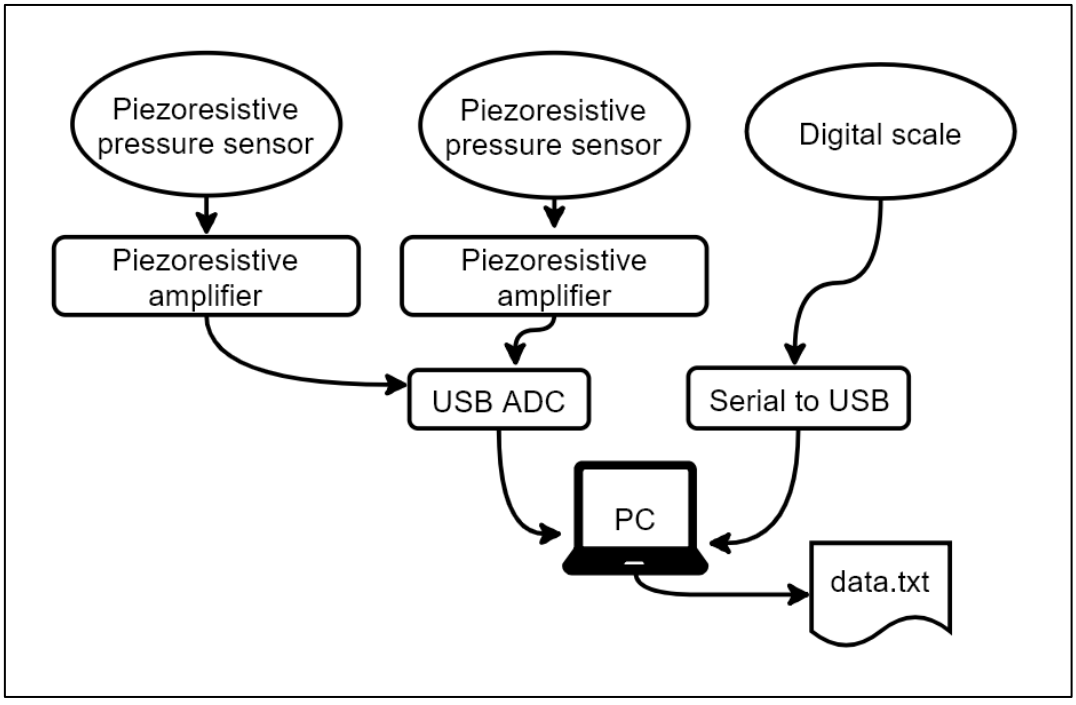

Figure 32 Data acquisition flow diagram. [Author]

3.3.2.1 DAQ Architecture

A basic LabVIEW virtual instrument (VI) was setup to capture and log data from two analog sources and a serial source. A makeshift *queued message handler* type system was implemented. Three parallel loops communicated through a queue and transferred and synced data through the same queue. The VI provided a user interface (UI) where data logging could be initiated and terminated. Real-time representations of the data in the forms of numeric displays and line graphs were also present in the UI. A new plain text file was created upon every data logging initiation. Elapsed time, inlet pressure, outlet pressure and scale reading were logged every 500 ms to the text file; the graphical plots in the UI were updated every 33 ms for smooth drawing. An example of raw data can be found in the *Data Analysis* section bellow.

3.3.2.2 Sensor Calibration

The piezoresistive sensor amplifier outputs were calibrated to a reference pressure meter, the testo 512. The outlet of the permeability testing apparatus was closed off after purging out the air with silicone oil; there were no fabric plies used during calibration, just an oil-filled chamber. The testo 512 pressure meter was pneumatically coupled to the air line just before the oil tank. The oil-filled system with a blocked outlet was then incrementally pressurized by adjusting the manual air pressure regulator. The direct current voltage (VDC) signals from the piezoresistive amplifier outputs were data-logged and the pressure readings from the testo 512 pressure meter were also noted. The recorded pressures were plotted, shown in [Figure 33], as a function of the logged voltages. Pressures under 250 mbar were omitted. A best fit line was used to derive the linear functions for voltage to pressure conversion. The linear functions were input into the VI's DAQ-assistant calibration settings.

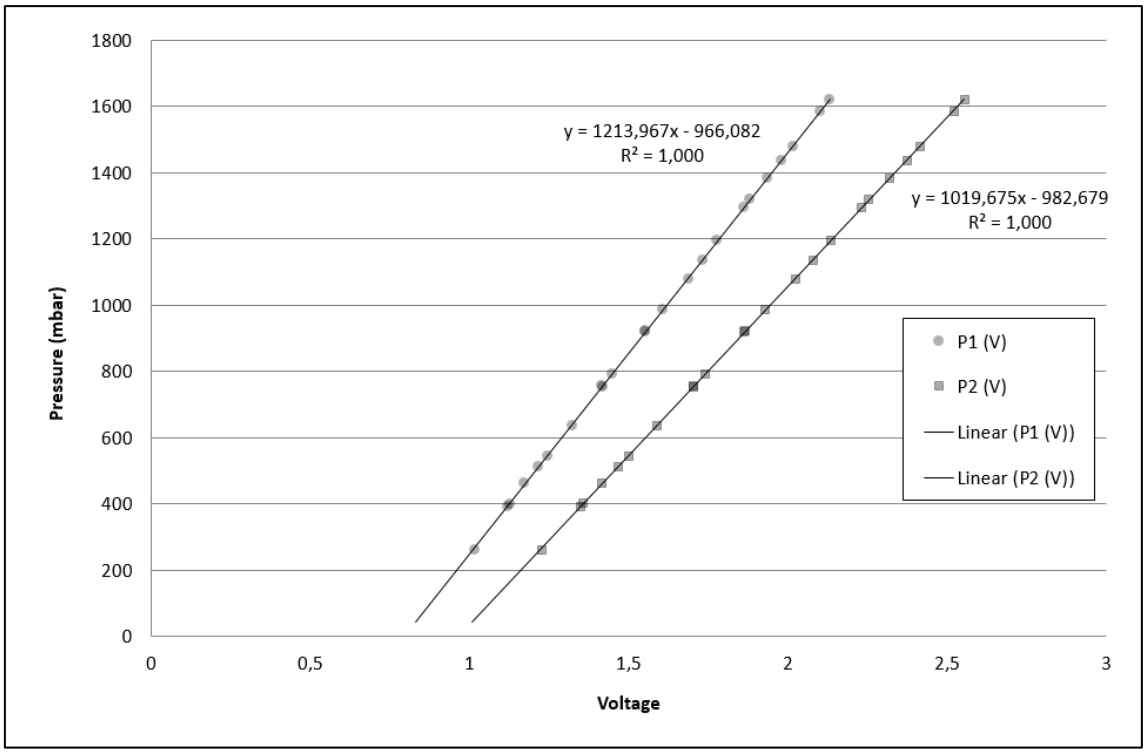

Figure 33 Amplifier voltage vs measured air pressure and best fit lines. [Author]

With minimal fitting deviation and high R-squared values the linear functions were deemed representative of the system. It should be noted that there seemed to be a direct correlation between recorded pressure and measured voltage, this would indicate that the function is not simply linear, however the deviations are orders of magnitude less than the estimated values. For use at pressures below 250 mbar the system should be re-calibrated.

3.3.3 Data Analysis

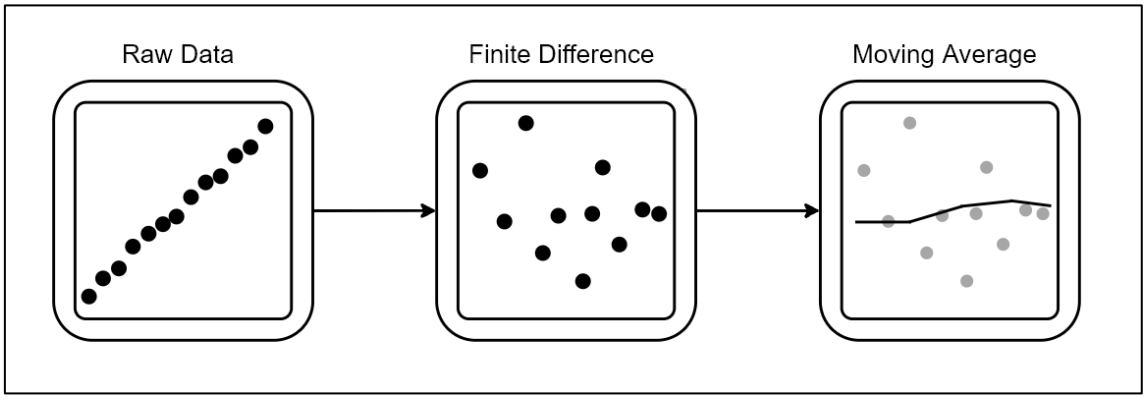

Figure 34 Data processing steps for mass flow rate from raw weight data. [Author]

3.3.3.1 Data Processing

Raw data in the form of text files were imported into a spread sheet application. A per-sample finite difference method was used to estimate mass flow rate from the measured weight, [Figure 34] . With the given density for the oil, volume flow was calculated per sample. Erroneously a density value of 925 kg/m^3 was used for all calculations instead of 965 kg/m^3, an error of about 4%. Inlet and outlet pressure differential was calculated by subtracting outlet pressure from inlet pressure per sample. Permeability was calculated per sample using Darcy's equation [eq. 1] with the assumptions of a homogeneously porous medium, constant fluid viscosity, constant height, constant area and fully saturated medium. See [Figure 35] for an overview of the raw data.

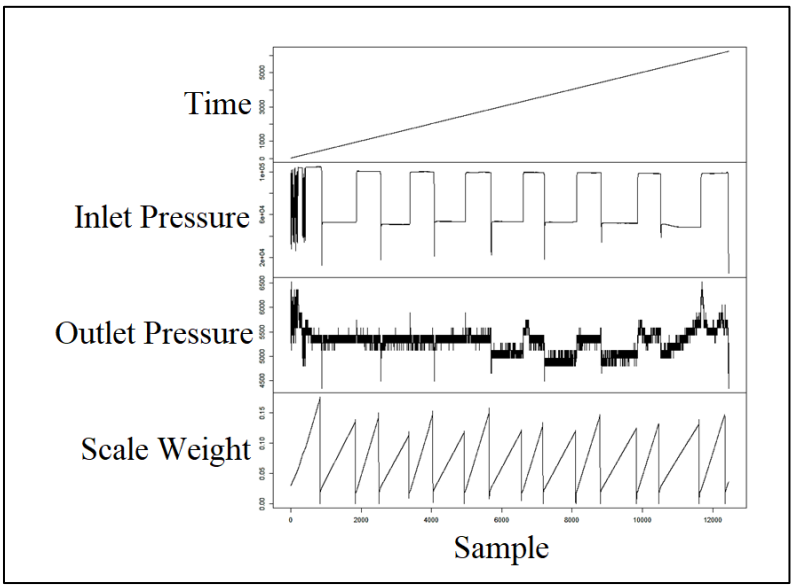

Figure 35 Raw data overview. Time was useful to visualize to make sure sampling times were constant. [Author]

3.3.3.2 Data Visualization

The finite difference method for mass flow resulted in apparently noisy data. This noise carried over into the permeability calculations. With the relatively high sampling rate used during data acquisition a two-dimensional point-cloud was built from thousands of data points. The points were set to very low transparency to form a sort of heat map shown in [Figure 36]. A clear line emerged from the heat map. As the noise was present in the *weight data*, it was assumed to originate from the digital weighing scale. When visually comparing point clouds, noise appeared to worsen at higher flow rates and the noise was banded in nature, this would indicate that there was some sort of quantization error. The datasheet for the KERN PCB scale *does* indicate that typical settling time is 3 seconds and the scale was used for continuous flow measurement.

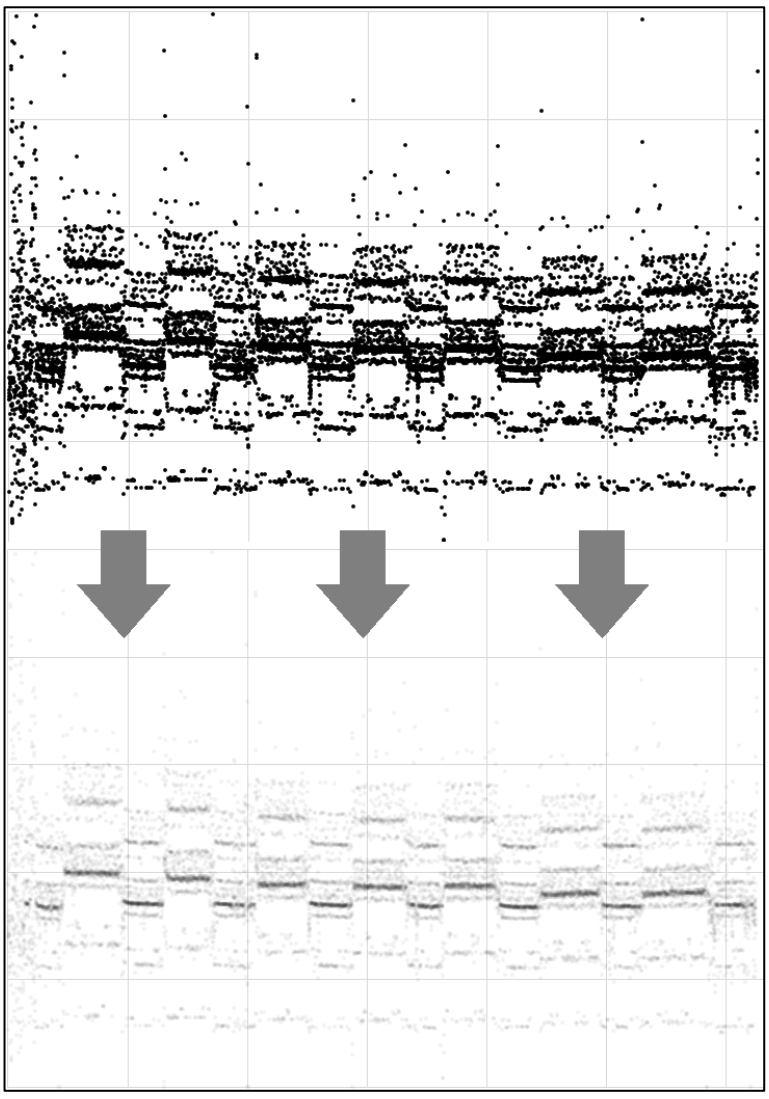

Figure 36 Point-cloud with transparency for data visualization. [Author]

By understanding the erratic nature of the noise and with clear hot spots in the data, a moving median filter with a centered window of about 100-200 samples was used to verify the nature of the point cloud distribution. The hot spots lined up with the median values shown in [Figure 37] and the rest of noise was some sort of gross, sporadic, deviation.

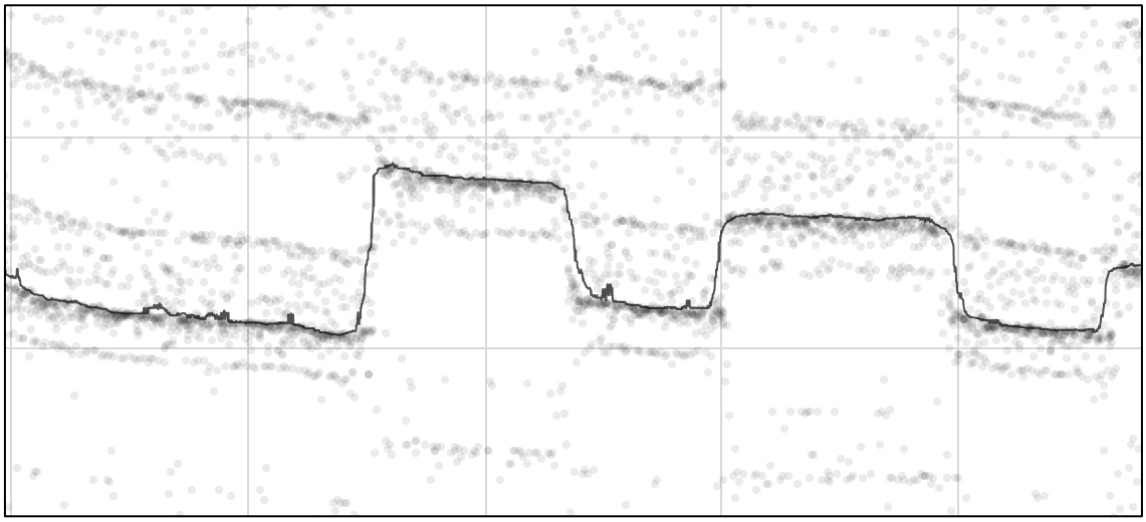

Figure 37 Median (solid line) filter following raw data (point-cloud). [Author]

Permeability values and measured pressure gradients were plotted against elapsed time to draw a relation between pressure and permeability. Permeability values within the dense, median, region were selected when comparing permeability of different fiber volume fractions or different pressure gradients. Due to the lengthy nature of the measurements and sensitivity to trapped air and ply layup, only about six semi-successful data sets over five different volume fractions were suitable for comparison.

3.4 Thermoplastic Plate Manufacturing

A series of fiber-reinforced thermoplastic plates were manufactured using a CRTM process in order to define process parameters for fully impregnated parts. The molded plates were later sectioned at areas of interest for closer examination.

3.4.1 Molding Process Variables

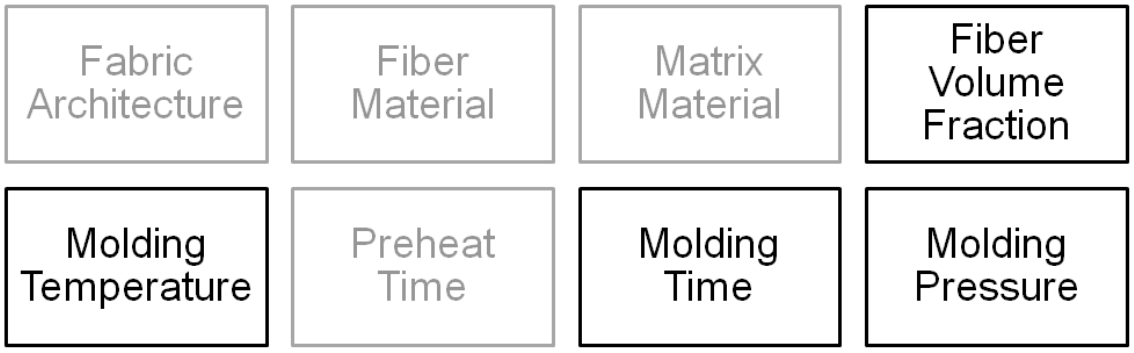

Figure 38 Compression molding variables overview. Grayed out variables were kept constant. [Author]

Molding temperature was varied to investigate the influence of melt viscosity. Differences in molding times were expected to show different stages of the infusion as well as different states of fabric relaxation. Molding pressure variation was used to explore the effects of fabric compaction. Fiber volume fraction was varied to increase or decrease preform permeability.

The same 1280 GSM leno-woven fiberglass fabric and black PA6 were used for all moldings as well as the same preheat time of 10 minutes to get the mold and its contents up to working temperature. The PA6 was dried in a vacuum oven and stored in a metallized film bag which was heat sealed and cut open and heat sealed again for each use. See [Figure 38] for a graphical overview of molding variables.

3.4.2 Molding Process Description

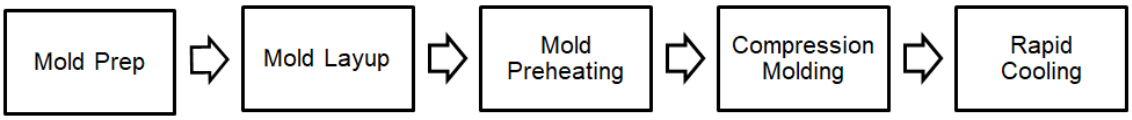

Figure 39 Compression molding flow chart. [Author]

[Figure 39] is a brief overview of the molding process. Mold layup started with the assembled and weighed preform of four plies. Given the preform weight, fabric density, and desired fiber volume fraction, the matrix weight was calculated. The calculated amount of matrix was poured first into the mold, distributed evenly and finally the preform laid on top. The mold was fully assembled by placing the core into the cavity. See [Figure 40] for a schematic view of the mold, fabric and matrix.

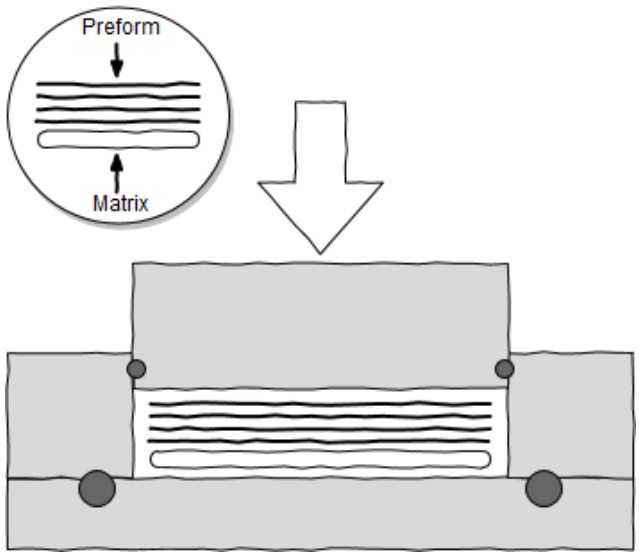

Figure 40 CRTM mold schematic with resin and fabric placement noted. [Author]

The heated press, drawn in [Figure 42], was set to the correct pressure and the heated plates to the desired temperature. The mold was inserted into the center of the heated side of the press along with two spacer bars for preheating. The spacer bars allowed the closing of the press without compressing the core and cavity. Once preheating was over the spacers were removed and the plate was compression molded by closing the press. After the compression time had elapsed the mold was transferred to the water-cooled side of the press and compressed at the same pressure. Demolding was carried out after about 10 minutes. of cooling.

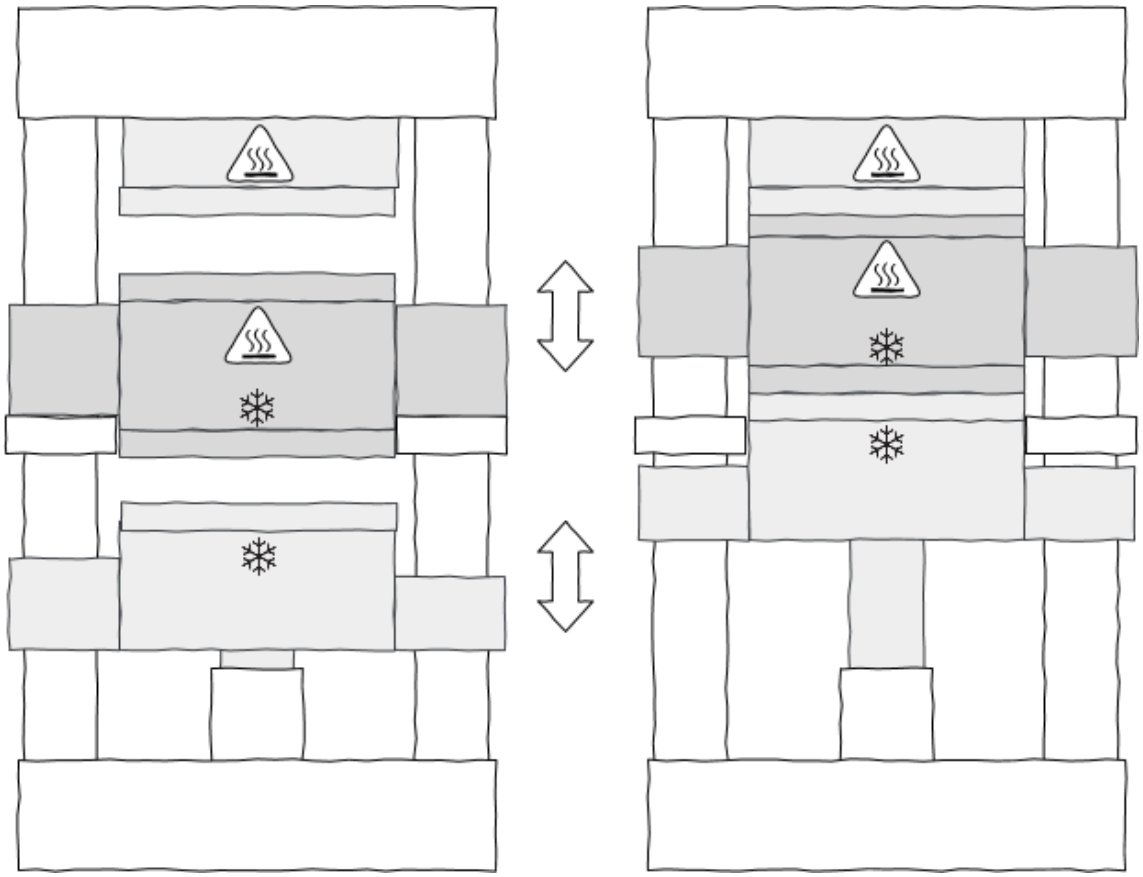

Figure 42 Heated and cooled hydraulic press drawing to supplement description. [Author]

The demolded and flash-trimmed plate was weighed and an average thickness measurement taken. The plate was labeled as shown in [Figure 41] with a serial number, plate weight and average thickness. Plate weight and average thickness were documented in the data logging spreadsheet. Photographs of individual plates were also taken.

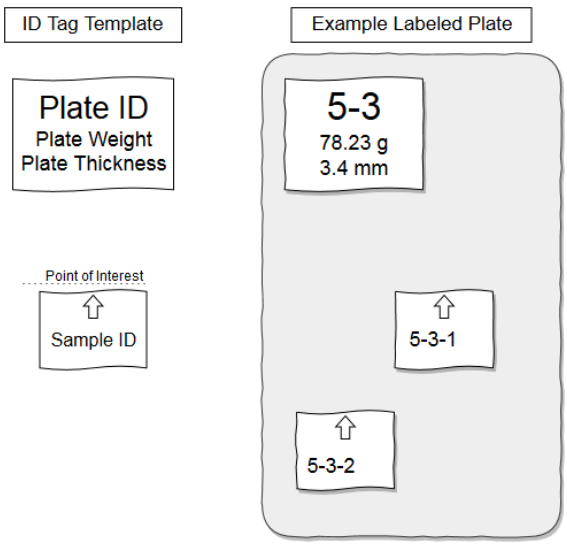

Figure 41 Example of sample labeling. [Author]

If the mold required cleaning it was disassembled, polymer blasted, and re-coated with release agent. If the previous demolding was troublesome the mold was usually cleaned and coated.

3.5 UV Fluorescence Microscopy

The molded plates were sectioned and infused with UV-fluorescent epoxy resin. The infused samples were extracted, embedded, and lapped. Finally, the lapped samples were lit with a UV source and photographed.

3.5.1 Sectioning

The fiber reinforced plates were examined for areas of interest and tagged for sectioning, see [Figure 41]. Areas of interest were identified through macroscopic visual examination. Most and least complete thermoplastic impregnated areas were often tagged as well as any other irregularities. Once tagged, the samples were cut by saw and the edges trimmed with a guillotine cutter pictured in [Figure 44]. To fit into the embedding molds, the samples were sized around 15 by 15 mm and the plates were under 5 mm thick.

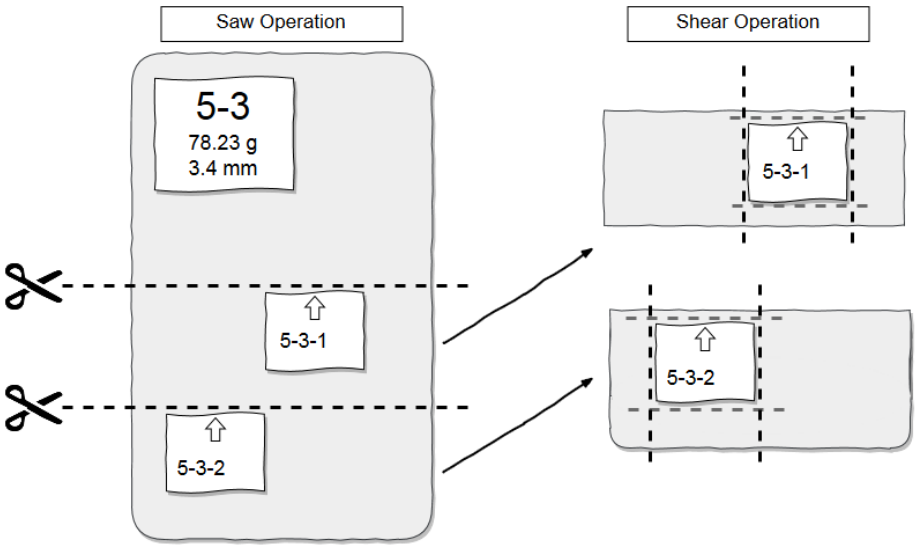

Figure 43 Visualization of sample sectioning. [Author]

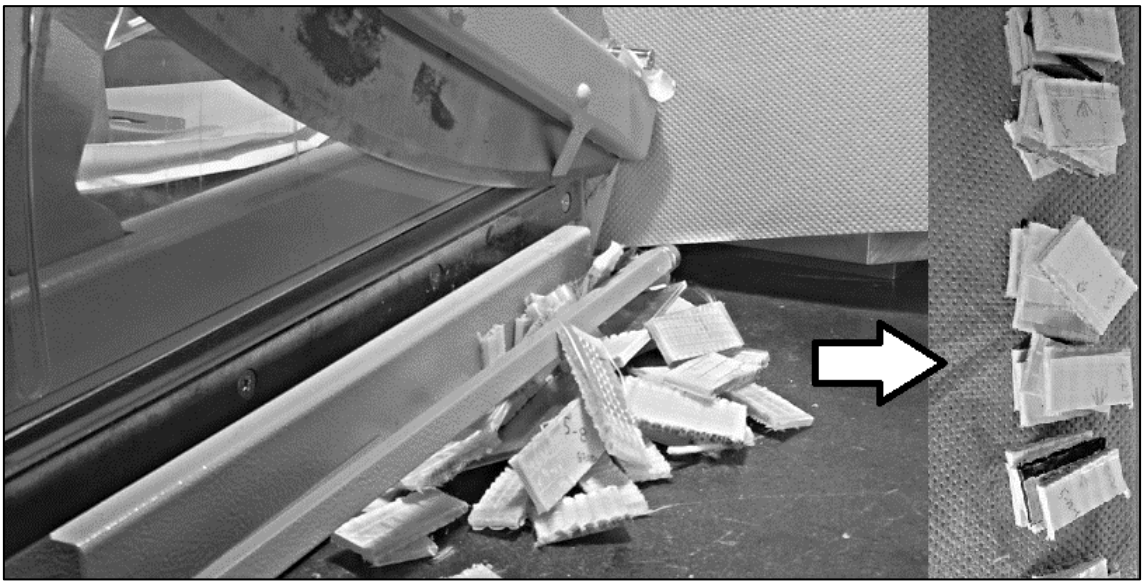

Figure 44 Paper guillotine cutting samples. [Author]

3.5.2 UV Fluorescent Resin Infusion

The same plate-molding tool was cleaned and re-coated with release agent. Tagged and sectioned pieces were placed into the mold shown in [Figure 45]. A gap of at least 5 mm from the area of interest was left to promote dyed resin ingress. The sample labels were placed facing the bottom of the mold where, after casting, the labels were most legible. The samples were taped down to prevent floating during the resin pour.

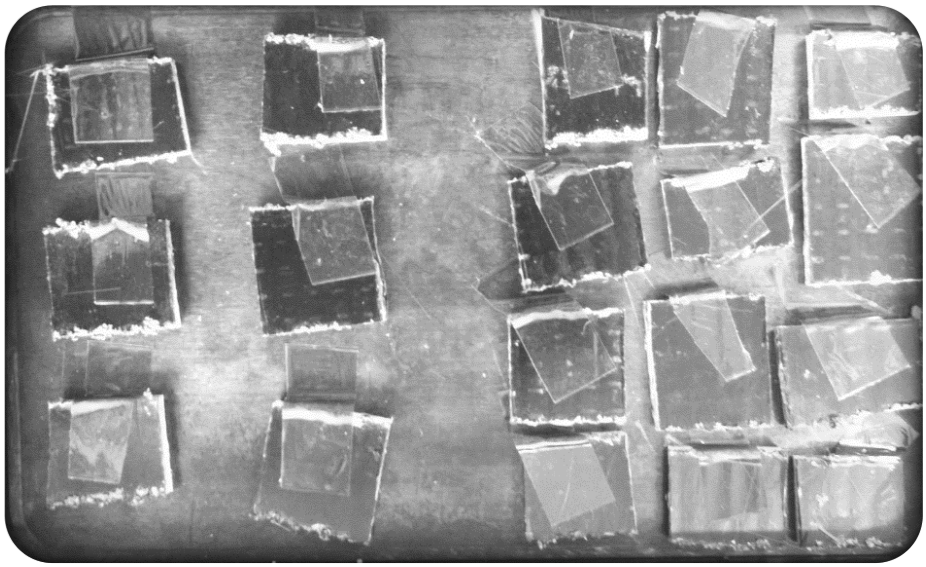

Figure 45 Picture of samples inside mold; taped down and ready for dyed resin infusion. [Author]

Rhodamine B was diluted into methanol at a mass ratio of about 1:10, rhodamine-to-methanol. The rhodamine-methanol solution was then diluted into clear epoxy resin at about 1:20. After an accidental serial dilution it was estimated that about 500 ppm by mass of rhodamine dye was used and produced a desirable result. Hardener was added to the dyed resin and mixed. The epoxy mixture was degassed under vacuum for under two minutes and then poured into the mold; enough to cover the samples. The mold was carefully assembled and again briefly degassed for under a minute.

The fully assembled mold filled with samples and dyed resin was placed in to a warmed hydraulic press with minimal closing pressure (~ 50˚ C and 10 bar). Once cured the samples were extracted from the epoxy plate shown in [Figure 46] by saw and finished up with a powered sander.

Figure 46 Fluorescent epoxy plate with embedded samples ready for extraction. [Author]

3.5.3 Sample Embedding and Polishing

The samples were then bedded into poly urethane pucks with sections-of-interest facing down. An initial, partial, pour was used to prevent the samples from floating during curing of the casting resin. Once the first pour gelled, the second pour filled the molds to an even height, completely covering the samples. Two-part polyurethane CEM 9000 casting resin was used as the embedding resin, gel time was about 3 minutes.

The fully cured pucks were then lapped and polished with an automated lapping and polishing machine pictured in [37, Figure 47]. A downward force of 15 N was used for wet grinding. A sample holder of about 120 mm in diameter was set to rotate at about 150 RPM in the same direction as the 250 mm in diameter grinding plate which was set at about 300 RPM. The grinding and polishing progression is tabulated bellow in [Table 1] and [Table 2].

Table 1 Grinding Grit Progression

Grit #	Lapping time (min)
220	1
500	2
1200	2
2400	2
4000	2

Table 2 Polishing Grit Progression

Polishing particle size (micron)	Polishing time (min)
3	4
1	4

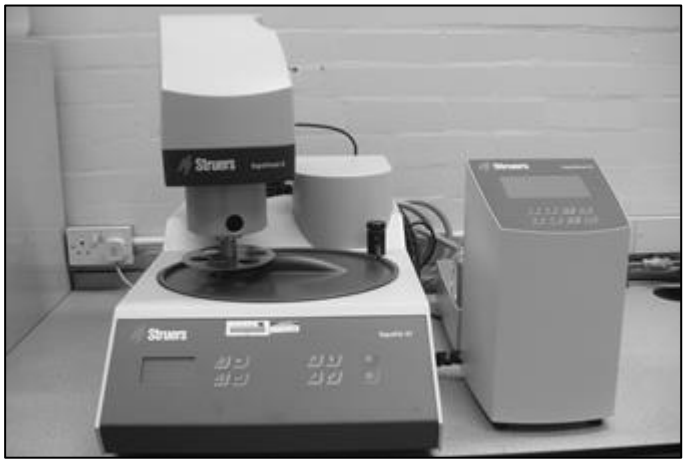

Figure 47 Example of automated lapping and polishing machine. [37]

3.5.4 UV Fluorescence Photography

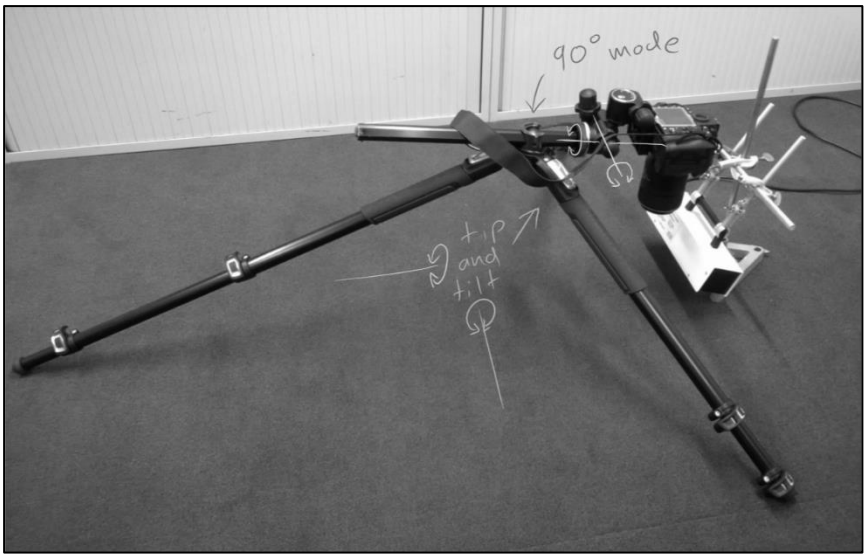

Figure 48 UV fluorescence photography setup. Camera, tripod, UV source and the ground. [Author]

A high-resolution Nikon D810 DSLR (Digital Single-Lens Reflex) camera was used with a 60 mm macro lens. A UVC light source was used to illuminate the surface of the sample in a completely dark room. It was found that UVC produced less bloom during imaging versus UVB. A black blanket over the camera and light source was used to block out stray light. Long exposure times, small aperture sizes and med-low sensitivity were used to maximize detail. The small aperture was needed for greater depth of field and the low sensitivity was needed to reduce sensor noise. To combat the low light and low sensitivity, exposure times in the order of 10-15 seconds were used. When attempting the same with a digital optical microscope with dated sensor technology, exposures can be in the order of minutes with multiple exposures. Samples were leveled onto a microscope slide with a leveling press to ensure that the sample surface was parallel to the plane of focus, see [Figure 49]. Vibrations were avoided by using shutter release timers and having both camera and sample rest on a monolithic surface, the ground as shown in [Figure 48].

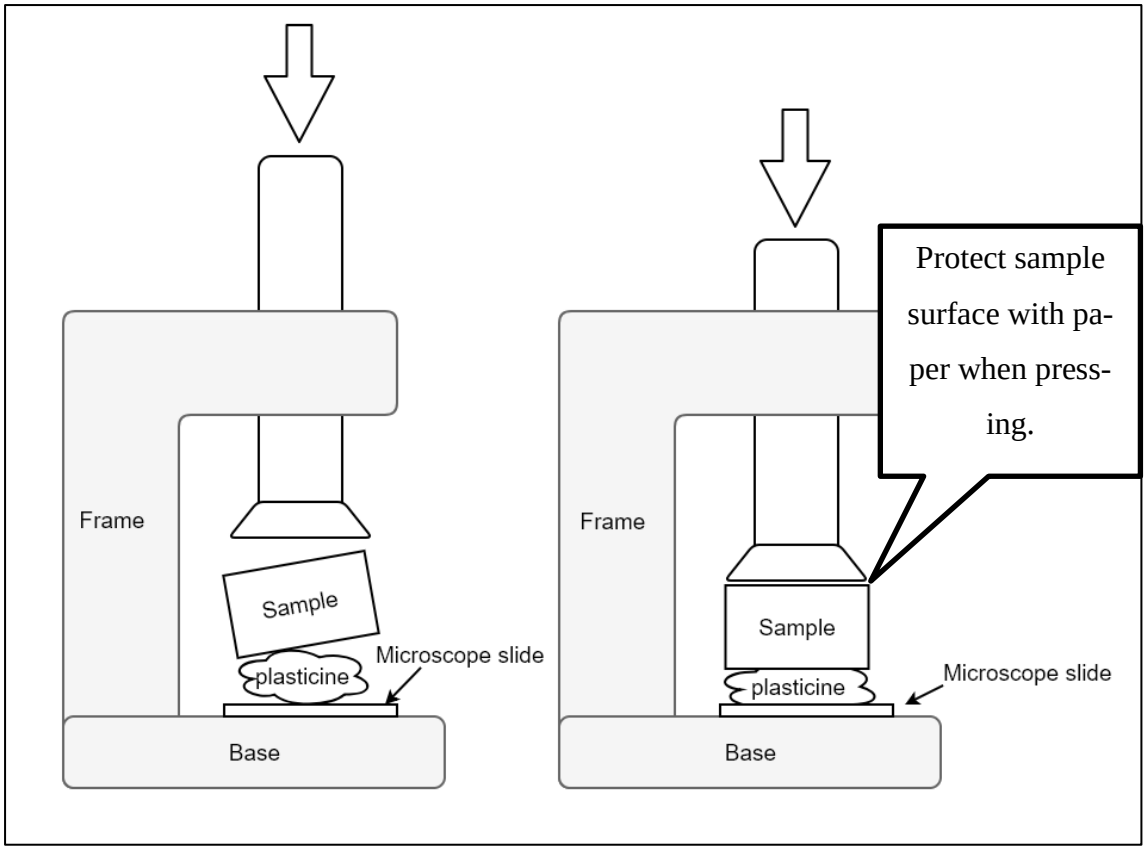

Figure 49 Workings of a leveling press used to level samples. [Author]

3.6 Excluded Materials

Although 540 GSM leno-woven NCF fabric is listed as a material, it was only used during preliminary testing. The specific prototype 540 GSM fabric was woven too loose and was not suitable for manual manipulation nor CRTM, the rovings flattened out during molding and a plate was never fully saturated, flattening shown in [Figure 50].

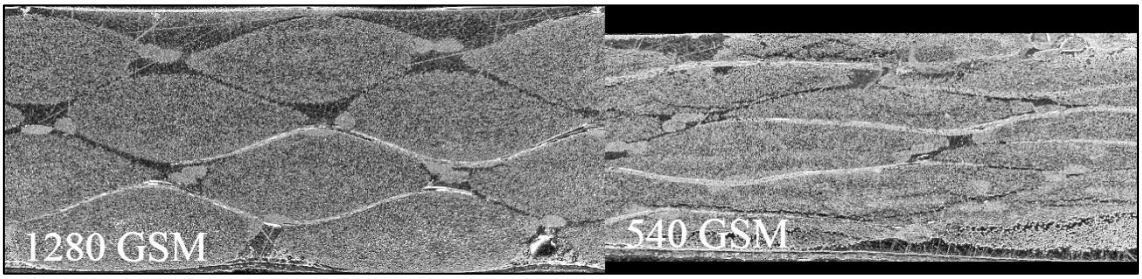

Figure 50 PP samples with 1280 and 540 GSM fabric. Note the lack of ordered nesting in the 540 GSM sample. [Author]

PP was also listed and indeed many samples produced, however the PP was translucent and made for very low contrast UV fluorescent images. The PP plates were also covered in what looked like significant crazing seen in [Figure 51].

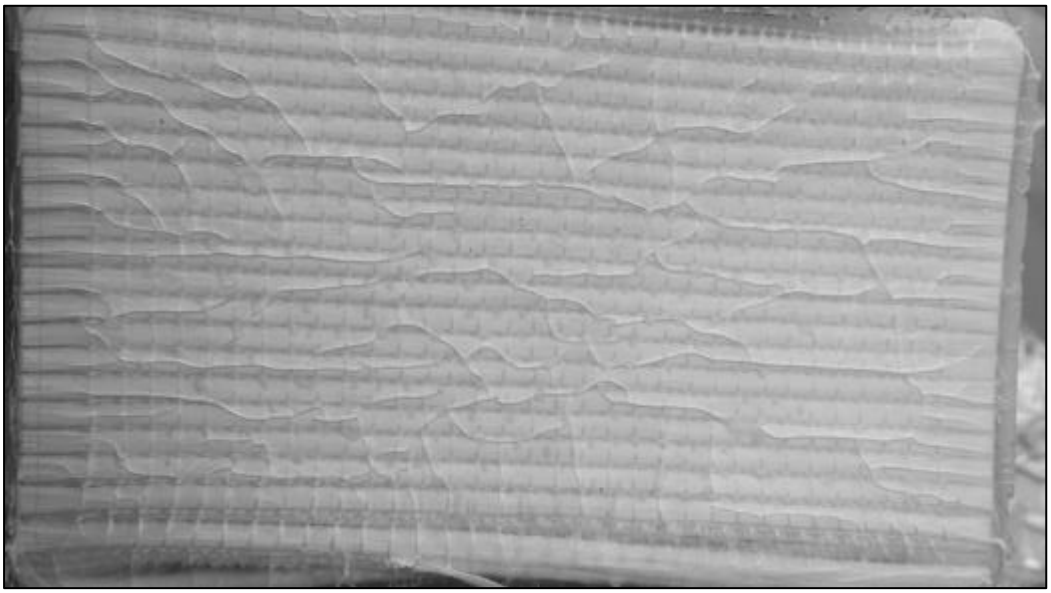

Figure 51 Crazing or cracking visible on PP plates [Author].

3.7 Fabric Analysis: Permeability

3.7.1 Complete Vf vs Permeability Overview

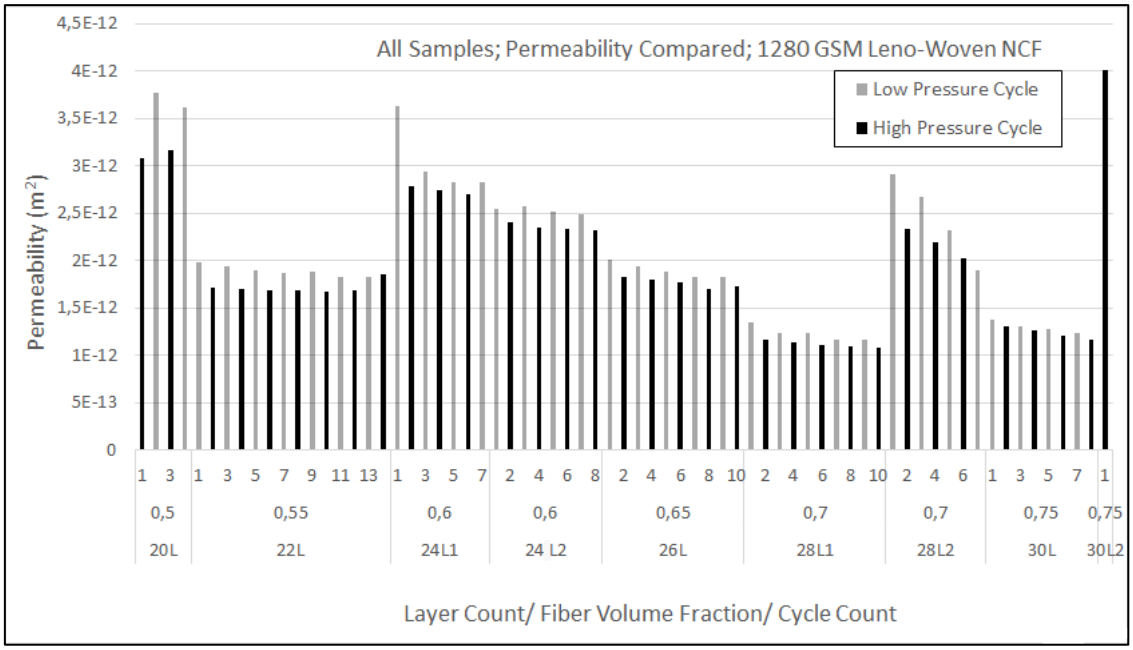

Figure 52 Permeability results of whole sample set. Each experiment and their individual cycles are plotted. [Author]

[Figure 52] shows permeability values derived from the raw data. The set includes all trials including those which exhibited unexpected flow rates or excessive air bubbles. A table, [Table 3], is provided to summarize the trials and any specific notes per trial. On a per-trial basis, permeability generally drops throughout the duration of the experiment. Higher resolution data is available in the *Fluid Pressure vs Permeability* section bellow.

Table 3 Permeability trials and their comments.

Layer Count	Calculated Vf	Cavity Height (mm)	Notes
20	0,49	20	
22	0,54	20	
24-1	0,59	20	Possible layer count of 22
24-2	0,59	20	
26	0,64	20	Air bubbles present during whole measurement
28-1	0,69	20	
28-2	0,69	20	Air bubbles present and apparent high flow rate
30-1	0,74	20	
30-2	0,74	20	Unusually high flow rate

Trials with unusually high, or low, flow rates were omitted for the next comparison set. The 24 layer test which was possibly 22 layers was also omitted due to a possible mis-count. If it was assumed to be 22 layers, the permeability numbers would fall in-line with the overall Vf vs permeability trend.

3.7.2 Selected Vf vs Permeability Trends

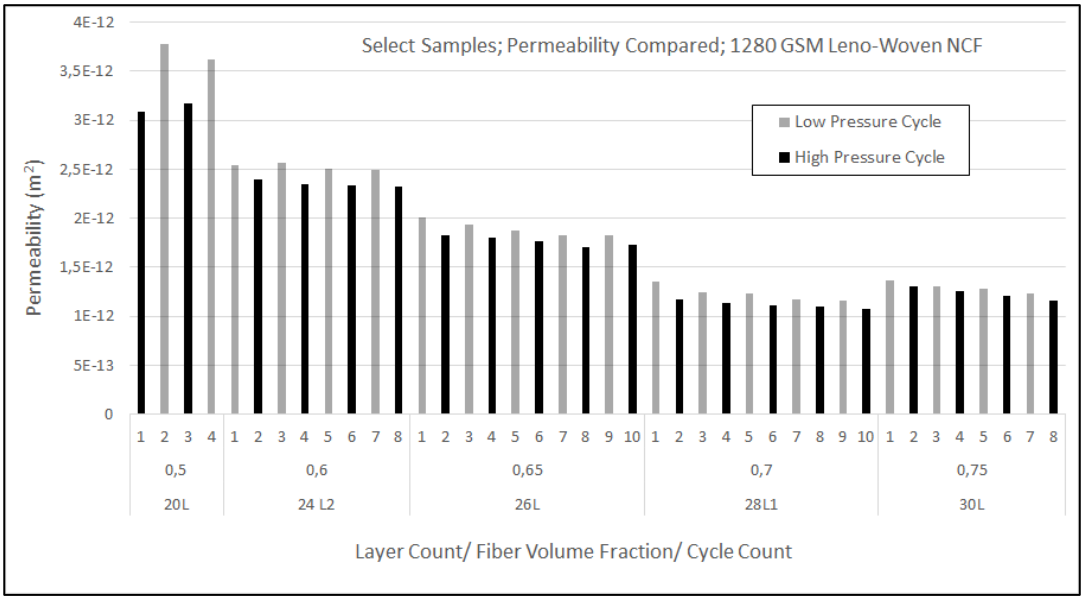

Figure 53 Select permeability trials. [Author]

Here in [Figure 53] with omitted trials, permeability drops as Vf is increased. Permeability decay is non-linear, permeability approaches a non-zero value at higher fiber volume fractions. The selected Vf range represents fiber volume fractions that would be used in industry.

3.7.3 Fluid Pressure and Permeability

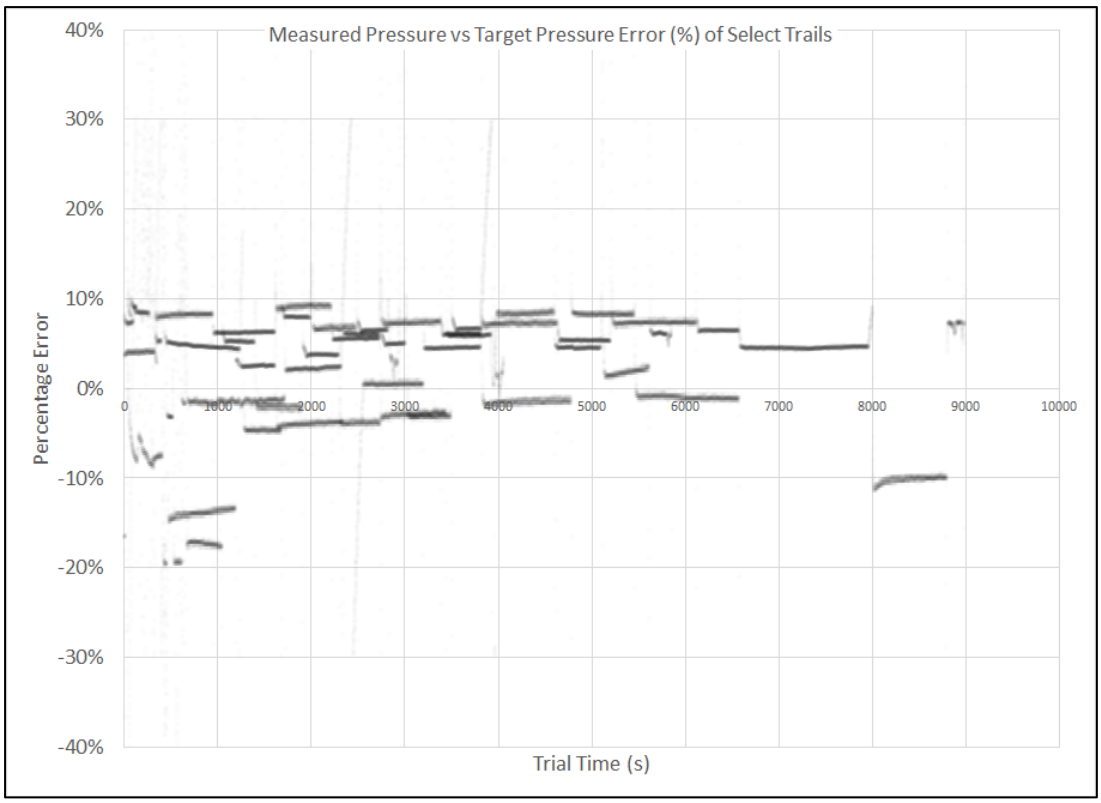

Figure 54 Pressure error from target of either 0,5 bar or 1,0 bar. [Author]

With manually-set air pressures, measured fluid pressures stayed within ±15% of the target of either 1,0 or 0,5 bar.

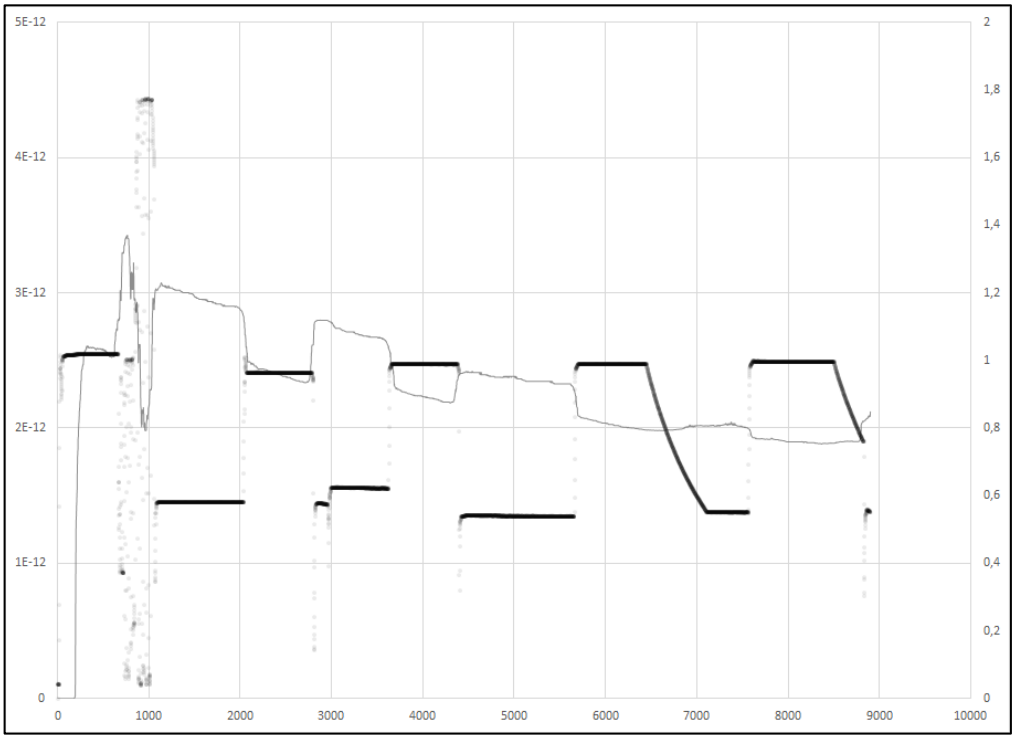

Figure 55 Inlet pressure and permeability over time. Notice a reluctance to lower pressure when venting was overlooked. Also notice the very stable pressure once set. [Author]

Once set, fluid pressure was kept very stable by the air pressure regulator as shown in [Figure 55]. It is also apparent that if venting is overlooked that pressure will not drop to the lower setting. Most samples displayed an overall trend of decreasing permeability throughout the experiment and there is a clear correlation between pressure and permeability however this correlation lessens as the measurement progresses.

3.7.4 Fluid Pressure Preform Compaction and Debris

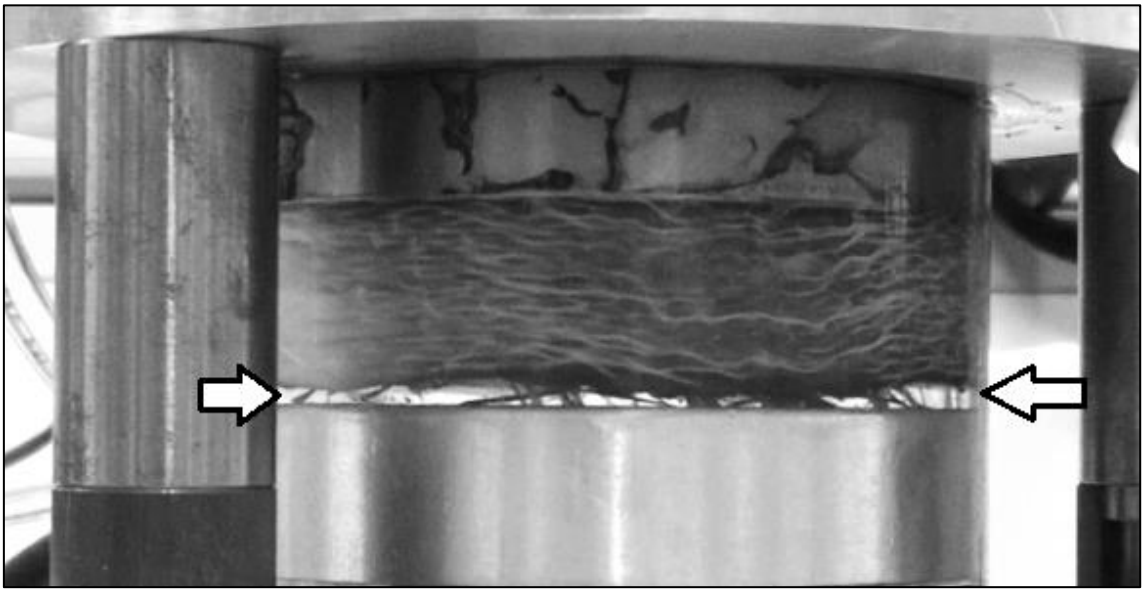

Figure 56 Preform stack lifting during permeability experiment. [Author]

The fabric stack was observed to compress under the pressure gradient in the test chamber at low volume fractions, see [Figure 56]. This change in height was not accounted for in the permeability calculations where the effect would be two-fold. The compacting fabric is essentially at a higher Vf which would result in lower flow, and the lower length would lower the value of the calculated permeability.

3.8 Macroscopic Analysis

Macroscopic Analysis will cover molding parameters used and the features of resultant thermoplastic parts.

3.8.1 Molding Statistics

All plates were molded using the same 1280 GSM UD leno-woven glass fabric and specialty low-viscosity PA6. A sample set of 20 plates is presented at two fiber volume fractions; 0,6 and 0,65.

3.8.1.1 Molding Parameter Spread

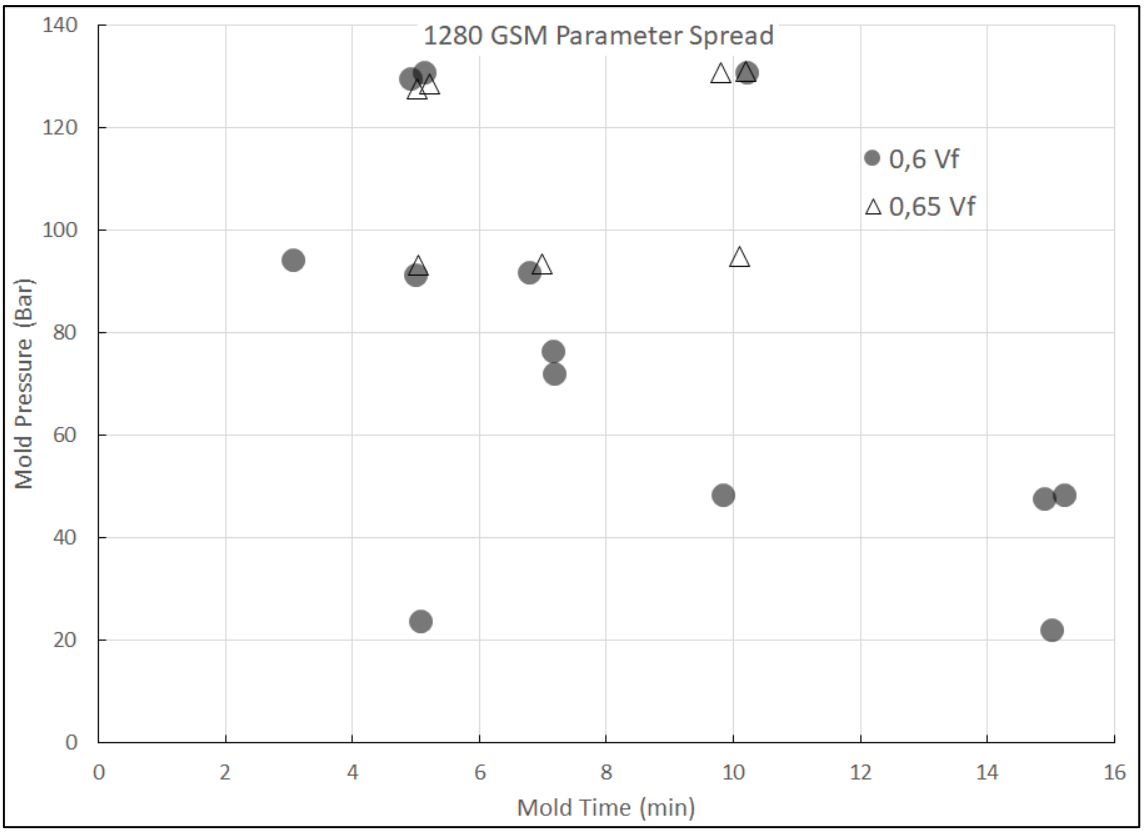

Figure 57 A scatter plot with random jitter introduced to visually separate discrete values. [Author]

At low compression times there was a tendency to use higher pressures and at higher times, lower pressures. Very few plates were molded outside this trend. Plates at 0,65 Vf were only molded at higher pressures. See [Figure 57] for parameter spread, the chart does not discern between different mold temperatures.

3.8.1.2 Plate Molding Statistics

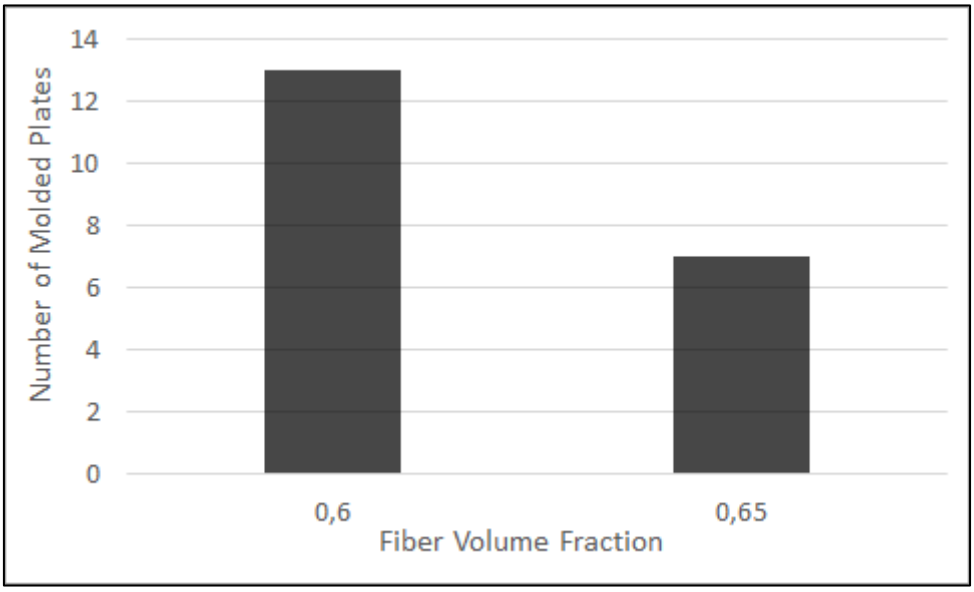

Figure 58 Number of pates molded per fiber volume fraction. [Author]

More than double the plates were molded at 0.6 Vf versus 0,65 Vf as shown in [Figure 58].

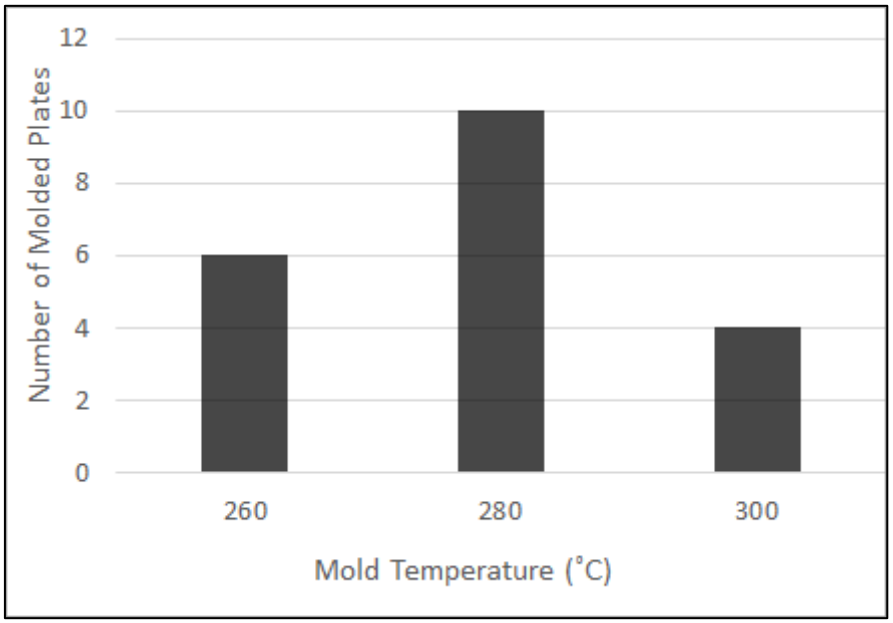

Figure 59 Number of plates molded per molding temperature. [Author]

Most plates were molded at 280˚ C, see [Figure 59]; at 300˚ C the mold would release vapor of some sort when decompressing the press and the fluoropolymer O-rings would show signs of degradation. At 260˚ C plates were less saturated.

3.8.2 Plate Features

The plates often featured one side with a thicker layer of matrix and the other side with more fabric visible, sometimes with spots of dry fabric, see [Figure 60].

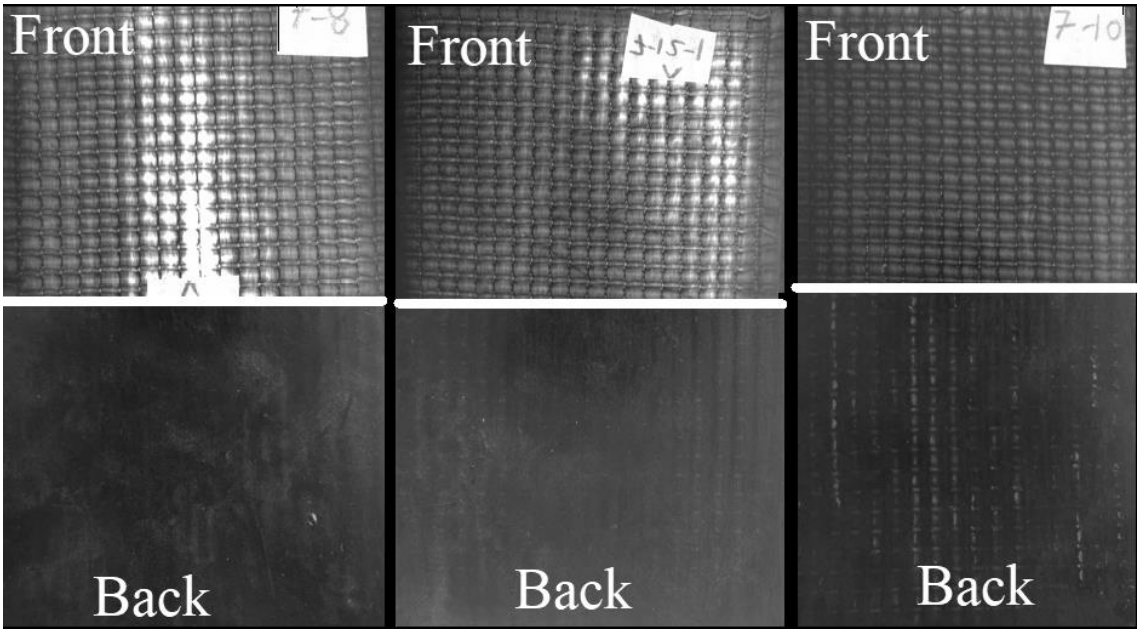

Figure 60 Front and back of plates with different levels of impregnation. [Author]

3.9 Microscopic Analysis

Usually it was the case that areas of least and/or most saturation were sectioned for closer examination. Even at higher molding pressures, where plates were the most saturated, there were areas of dry fabric which were sectioned. The sections do not represent the state of the whole plate.

The following images have not been normalized in any specific way to compensate for lighting, exposure, or other photographic attributes. The photos have been adjusted manually to similar exposure levels. Larger images can be found in the appendix.

3.9.1 Visible Features

With the UV fluorescence methods many features are clearly visible, see [Figure 61]. Rovings are outlined, voids are bright and individual fibers are almost discernible. The visible cracks in some samples could have been introduced during the sectioning process, from either sawing or shearing, or both.

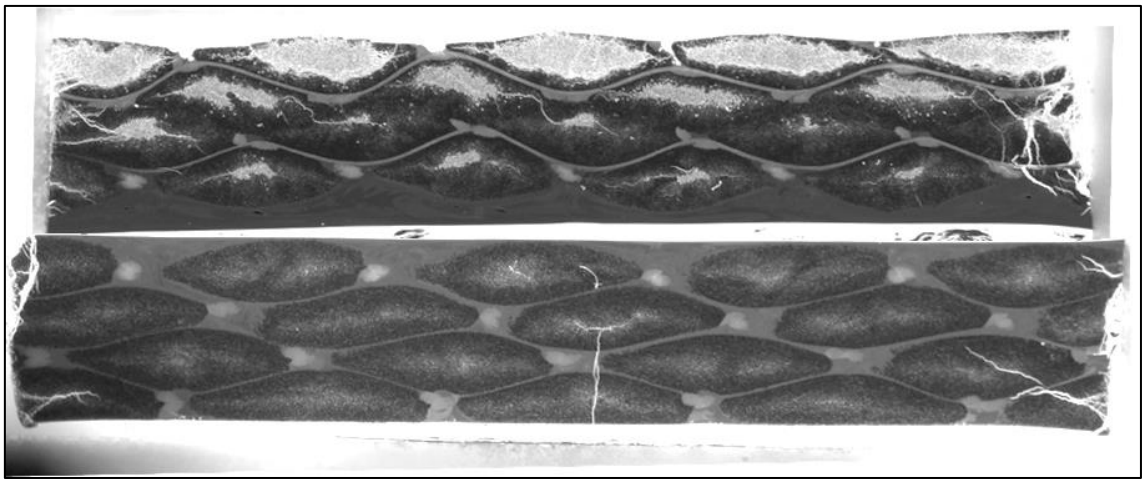

Figure 61 Sample of features visible with UV fluorescence imaging. [Author]

3.9.2 Cross Section Overview

Water-like surface contamination emerged during storage in a few samples that show up as paint streaks in the UVC-lit images. It isn't clear from where the contamination originated from, possibly secretions from the two-part resins used for dyeing and embedding.

A gradient of saturation is observed in partially saturated samples. Saturation is greatest from the side of matrix impregnation. Bundled compaction also follows this gradient, being more compact at areas of highest saturation.

Nesting patterns are also present. Most samples show pyramidal nesting where the rovings on top nest in between the rovings bellow. One of the 300˚ C samples show two center layers stacked in a serial fashion where the top rovings are aligned right on top of the rovings bellow. There was no strong correlation between molding parameters and nesting behavior nor roving deformation.

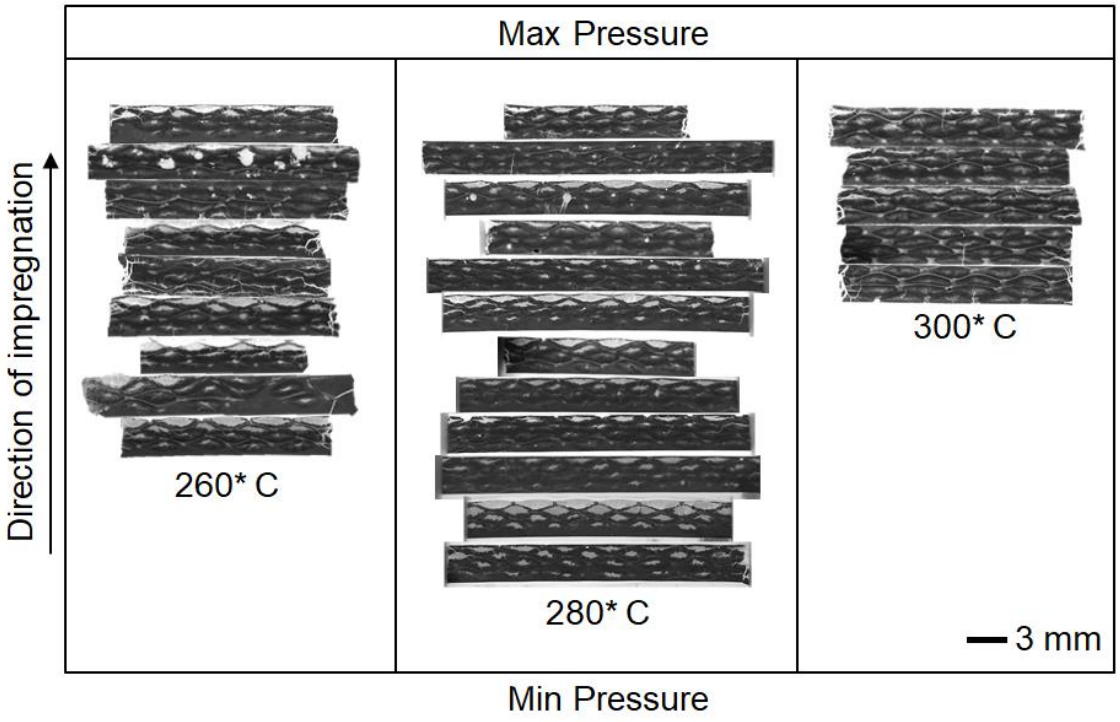

Figure 62 Overview of all cross-sections. [Author]

While the 300˚ C samples seem most uniformly saturated and compacted, they still exhibit the common feature of a brighter center of the roving. The brighter center suggests void content. The relatively high saturation levels of the 300˚ C samples are attributed to the lower viscosity of the PA6 melt at the higher temperature.

Across all samples, void content is most apparent in the center of the rovings. This would indicate a dual-scale flow where the bulk of the melt passes around the spaces in between rovings and at a slower rate saturates spaces between individual fibers within the rovings. The farther these central voids are located from the side of matrix impregnation, the larger they are.

3.9.3 Plotted Cross Sections

Longer mold times produced more saturated parts; this effect was most apparent with low mold pressures. At higher pressures, time is less of a factor and short mold times can yield equally saturated parts. Larger versions of [Figure 63] are found in the appendix.

[37]

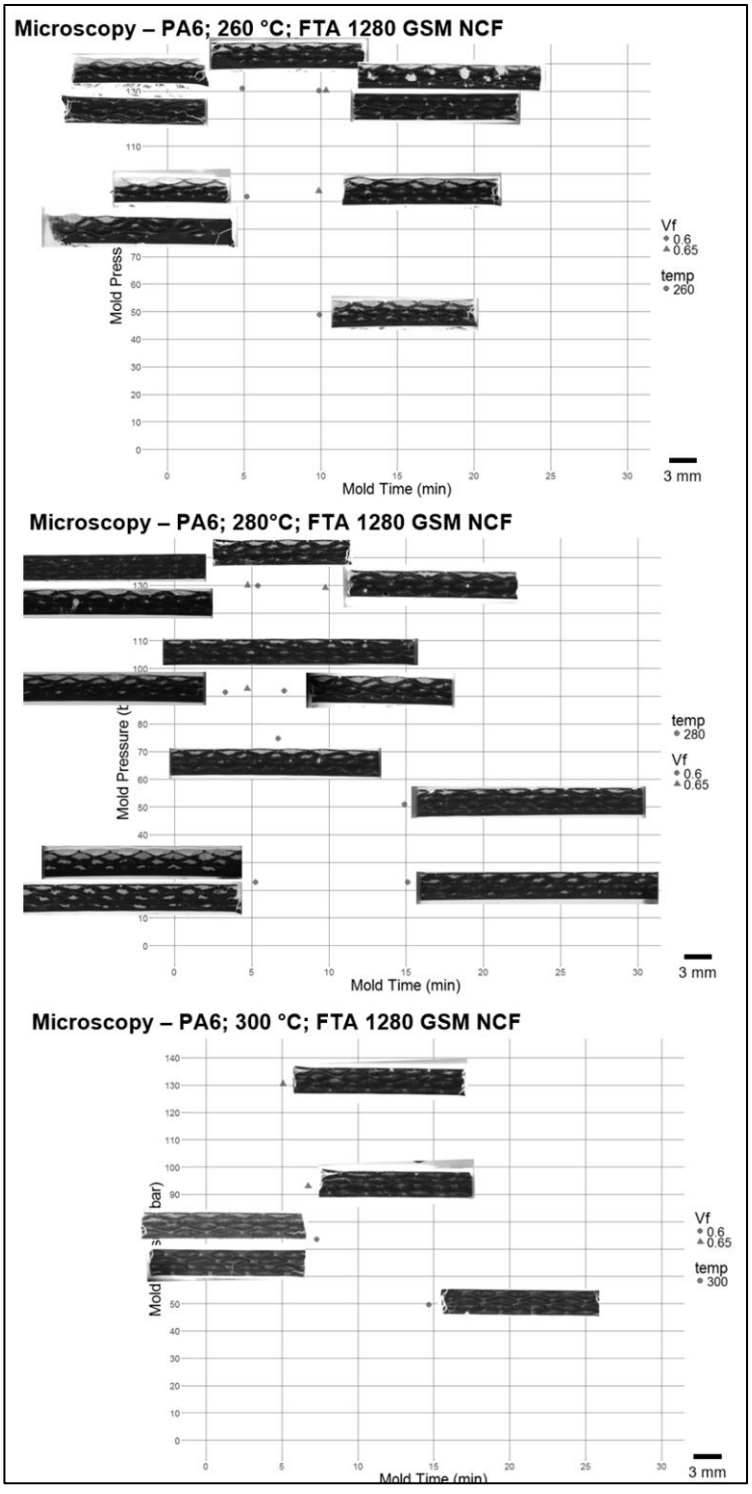

Figure 63 Cross-sections plotted against mold time and pressure. [Author]

4 DISCUSSION

4.1 Summary

Highly variable permeability measurements revealed an inverse relationship between fluid pressure and permeability, fabric permeability was not static. Compression molding results were most influenced by molding pressure and temperature; high pressures and high temperatures resulted in lower void content. High contrast void detection with UV fluorescent imaging was achieved with low dye concentrations and UVC excitation.

4.2 Implications

The FTA leno-woven all-glass NCF maintained high enough permeability for complete low-viscosity thermoplastic compression molding. During compression molding, the exerted pressure would have compacted the fabric, reaching a minimum permeability state. The minimum permeability state during molding was greater than zero and high enough to allow for successful molding. It is the compaction behavior and stability of the fabric which contributed to the effects witnessed.

The straightforward methods and high-contrast images provided by the UV fluorescent microscopy allows for quick capture and visual void analysis of the molded plates. The high-contrast nature of the images should simplify future implementations of machine vision for quantitative void analysis.

4.3 Considerations, Limitations and Notes

4.3.1 Permeability Testing

A few patterns emerged during permeability testing. From trial to trial there were large variations in measured permeability due to hugely varied flow rates. During trials it was observed that permeability continues to decrease as the experiment progresses over at least an hour. Permeability was also directly affected by the fluid pressure; higher permeability resulting from lower pressures and lower permeability at higher pressures.

Large variations have been attributed to variance of the fabric samples themselves caused by storage conditions and inherit non-uniformity of the fabric. Layer orientation, nesting, race tracking, damage from handling, and trapped air all might contribute to the large variations in permeability measurements as mentioned in [27].

Decreasing permeability over the experiment cycle might have been caused by the stack of layers and fibers slowly nesting into a more compact, less permeable state. It was also observed that the recycled oil was contaminated with sub-millimeter debris including fibers. Acting as a filter, the fabric stack might have been filtering out the debris in the oil and slowly decreasing in permeability due to blockages of fluid paths.

The relationship of fluid pressure and permeability can be explained by the fabric stack deforming under pressure. Lowering the height and increasing fiber volume fraction makes for a more dense medium for the fluid to pass through. Also at higher pressures the increased flow rate would require higher fluid velocities through the fabric which might contribute to higher resistance, explaining the decrease in permeability.

The permeability experiments required constant supervision, manual assembly and trial duration was about an hour on average. The silicon oil was very difficult to clean up and generally messy. For an experiment which requires large numbers of trials the setup has room for improvement.

While automation and assembly jigs would improve the current setup, ultimately an experiment that simulates the CRTM process would be more suitable and would be able to test both saturated and unsaturated permeability. Something syringe-like in nature would seem appropriate as well as using higher viscosity fluid to simulate the thermoplastic and pressures involved more accurately. Often water based fluids such as glucose syrup have been for testing permeability as stated in [40].

In any setup, race tracking at the edges of the test chamber would need to be dealt with. A specimen with a larger projected area would result in a lower ratio of perimeter to surface area. Pre-assembled preforms with resin-sealed edges could eliminate race tracking and lost rovings from edges; this would assume that race tracking was measured to be enough of an inconvenience to warrant more extreme measures.

When using clear fluid and glass fabric it was difficult to judge the level of saturation during and after testing. Dyed or marked fluid could be used to visualize flow and indicate saturated and unsaturated areas. This would probably make recycling the oil more difficult.

Using a digital scale that has a settling time of 3 seconds to measure continuous mass flow resulted in very noisy data and required frequent fluid receptacle changes. At dedicated flow meter might be a suitable replacement.

Efforts were made to dislodge trapped air out of the system by cycling air pressure quickly. Pulling a vacuum on the system would have reduce time spent clearing out air and achieved proper saturation as mentioned in [41].

There seemed to be a check valve located between the oil tank and the air pressure regulator. Lowering pressure at the regulator had a very delayed effect on the rest of the system. Increasing pressure at the regulator had an immediate effect. For the pressure to drop in the oil tank, air was vented from the oil tank and then air pressure allowed to build back up to the new, lower, set-point.

4.3.2 Thermoplastic Compression Molding

Overall the fabric properties made it possible to mold. The fabric remained intact, maintaining roving separation and whole, uninterrupted, rovings. There was evidence of highly dual-scale flow with the polymer melt passing through the whole preform but not fully saturating rovings farthest away from the injection side. Where present, voids were always found at the center of rovings.

In some cases, there was a higher gradient of roving compaction in the final part. Towards the injection side the rovings are flattened while rovings farthest away were most tall. It is speculated this is a case of fabric compaction where the injection side fabric experiences a higher pressure and the layers following are cushioned by the melt and surrounding fabric.

It was common to have one end of the plate with much more saturated fabric than the other end. Theories as to why include uneven pressure from the core/cavity racking or

generally being out of parallel. Possibly this is caused by trapped air or dimensional irregularities in the mold. The mold was placed centered to the hydraulic press plates to avoid any racking from the press. The press had massive bearing support in all four corners to prevent racking and was assumed to be parallel.

The fabric plies were cut in a way where the UD orientation was lengthwise with the mold. This made the weakest edges of the UD fabric also the longest. Rotating the fabric orientation by about 30 degrees would locate the weak edges of the fabric to two opposing corners of the mold, minimizing the almost sacrificial edge rovings.

There was a distinct vinegar-like odor when opening semi-sealed containers of molded plates. The odor was also present when molding PP plates at 220˚ C. One suspect source might be the degradation of the fiber sizing which was not intended for such high temperature molding. Another source could be some degradation of the release agent, although it was specified for the molding temperatures.

4.3.3 UV Fluorescence Imaging

Initial use of rhodamine B to dye resin and mark voids utilized too high a concentration of the dye. Through accidental serial dilution it was determined that much lower concentrations were more effective. The fluorescence was weaker and more blue to the naked eye. At higher concentrations the fluorescence was more red and possibly too intense, washing out some features of the specimen.

Exciting the samples was first done with a UVB source since the fluorescence was much brighter to the naked eye. When trying a UVC source, out of curiosity, a much more localized, more blue, fluorescence was observed. The images seemed to yield much more detail, highlighting features and hair-line cracks that were previously not clearly visible. It is speculated that the UVC is more easily blocked by the fibers and matrix material making them darker compared to dyed, resin-filled, voids. UVC could also be penetrating less deep into the specimen and scattering more than UVB. Rhodamine B has shown more absorption towards UVC wavelengths in (cite). This combination of thin depth of excitation and the more blue fluorescence might be why the contrast was much higher, showing more detail. Also, the fluorescent blue light was probably less likely to bleed through the red dye and specimen material.

With optical filters there might be even more contrast to be extracted from this method. This preliminary investigation could provide hints as to how to set up a fluorescence microscope if desired.

It helps when the materials aren't transparent to the wavelengths that are trying to be imaged. Natural PP and glass fibers made for very low contrast images as the whole sample lit up. A black matrix makes for good contrast.

The combination of a large-sensor DSLR camera and 60 mm macro lens resulted in a lot of wasted data as the in-focus sample only covered about 10% of the image area. Even though the high-resolution images allowed for a detailed look, there is a lot of room for improvement.

4.4 Suggested Further Investigations

Impregnation tests where viscous fluid is forced through a stack of dry fabric could be used to closely monitor fabric behavior and involved injection forces. The fluid viscosity would be that of the polymer melt and the test chamber built with a view to the fabric stack.

Mechanical tests on the molded plates or dedicated TP-CRTM test samples would reveal how structurally sound the parts are. Molding parameters could be compared to mechanical properties. Ultimately vertical injection molding tooling could be used for molding the samples.

The UV imaging method should be compared to other void analysis methods and find the limits of the imaging technique.

4.5 Conclusion

With crude molding methods, fully consolidated fabric-reinforced thermoplastic composite plates were molded. Successful plates were molded with relatively short compression times of 5-7 minutes. With further investigation into the mechanical properties of these composites, it is conceivable that refined versions of the TP-CRTM process will find their

way into high-volume industries such as the automotive industry. The key being the combination of relatively low viscosity thermoplastic and stable and permeable fabric architecture.

The UV fluorescence imaging appears to be effective and the method itself uncomplicated and accessible. Although the images are vibrant and seemingly distinguish voids, the method should be compared with other validated methods of void analysis.

REFERENCES

[1] United States Environmental Protection Agency, “Sources of Greenhouse Gas Emissions,” *Sources of Greenhouse Gas Emissions*, 25-May-2018. [Online]. Available: https://www.epa.gov/ghgemissions/sources-greenhouse-gas-emissions. [Accessed: 25-May-2018].

[2] U.S. Department of Energy, “Fact #880: July 6, 2015 Conventional Vehicle Energy Use: Where Does the Energy Go?,” 06-Jul-2015. [Online]. Available: https://www.energy.gov/eere/vehicles/fact-880-july-6-2015-conventional-vehicle-energy-use-where-does-energy-go. [Accessed: 25-May-2018].

[3] C. Bjelkengren, “The Impact of Mass Decompounding on Assessing the Value of Vehicle Lightweighting,” Massachusetts Institute of Technology, 2008.

[4] C. Dallner, “Materials for the Future of Lightweight Construction.”

[5] T. Renault, “Developments in thermoplastic composites for automotive applications,” 2015.

[6] *Regulation (EC) No 443/2009 of the European Parliament and of the Council of 23 April 2009 setting emission performance standards for new passenger cars as part of the Community’s integrated approach to reduce CO 2 emissions from light-duty vehicles (Text with EEA relevance)*. 2009.

[7] *Directive 2005/64/EC of the European Parliament and of the Council of 26 October 2005 on the type-approval of motor vehicles with regard to their reusability, recyclability and recoverability and amending Council Directive 70/156/EEC*. 2006.

[8] F. C. Campbell, “Introduction to Composite Materials and Processes: Unique Materials that Require Unique Processes,” in *Manufacturing processes for advanced composites*, .

[9] S. G. Advani and K.-T. Hsiao, “Introduction to composites and manufacturing processes,” in *Manufacturing Techniques for Polymer Matrix Composites (PMCs)*, Elsevier, 2012, pp. 1–12.

[10] S.-J. Liu, “Injection molding in polymer matrix composites,” in *Manufacturing Techniques for Polymer Matrix Composites (PMCs)*, Elsevier, 2012, pp. 15–46.

[11] F. C. Campbell, “Fibers and Reinforcements: The String That Provides the Strength,” in *Manufacturing processes for advanced composites*, .

[12] E. M. Sozer, P. Simacek, and S. G. Advani, “Resin transfer molding (RTM) in polymer matrix composites,” in *Manufacturing Techniques for Polymer Matrix Composites (PMCs)*, Elsevier, 2012, pp. 245–309.

[13] F. C. Campbell, “Thermoset Resins: The Glue That Holds the Strings Together,” in *Manufacturing processes for advanced composites*, 2004.

[14] F. C. Campbell, “Thermoplastic Composites: An Unfulfilled Promise,” in *Manufacturing processes for advanced composites*, 2004.

[15] F. C. Campbell, “Chapter-9-Liquid-Molding-You-Get-a-Good-Preform-and-Tool-You-Get-a-Good-Part.pdf,” in *Manufacturing processes for advanced composites*, .

[16] S. Bickerton and P. A. Kelly, “Compression resin transfer moulding (CRTM) in polymer matrix composites,” in *Manufacturing Techniques for Polymer Matrix Composites (PMCs)*, Elsevier, 2012, pp. 348–380.

[17] T. Creasy, “Sheet forming in polymer matrix composites,” in *Manufacturing Techniques for Polymer Matrix Composites (PMCs)*, Elsevier, 2012, pp. 123–138.

[18] J. A. Sherwood, K. A. Fetfatsidis, J. L. Gorczyca, and L. Berger, “Fabric thermostamping in polymer matrix composites,” in *Manufacturing Techniques for Polymer Matrix Composites (PMCs)*, Elsevier, 2012, pp. 139–181.

[19] G. Entholzer, “Engel Centre for Lightweight Composite Technologies Presentation,” Feb-2013.

[20] T. Hogger, P. Winkler, and T. Wehrkamp-Richter, “MAI SKELETT / MULTISKELETT A NOVEL DESIGN PHILOSOPHY BASED ON TRUSS ELEMENTS,” p. 9, 2016.

[21] L. Zingraff, V. Michaud, P.-E. Bourban, and J.-A. E. Månson, “Resin transfer moulding of anionically polymerised polyamide 12,” *Compos. Part Appl. Sci. Manuf.*, vol. 36, no. 12, pp. 1675–1686, Dec. 2005.

[22] M. BITTERLICH, “T-TRM_pa6.pdf,” *Kunststoffe*, vol. 3, no. 2014, pp. 80–84, 2014.

[23] S. Job, G. Leeke, P. Mativenga, S. Pickering, N. Shuaib, and G. Oliveux, “Composites Recycling Report 2016,” Composites UK Ltd.

[24] T. Tiedt, “Recycling carbon fibre waste,” Institut für Textiltechnik (ITA) der RWTH Aachen University Otto-Blumenthal-Str. 1, 52074 Aachen, Germany.

[25] T. Miyake and S. Imaeda, “A dry aligning method of discontinuous carbon fibers and improvement of mechanical properties of discontinuous fiber composites,” *Adv. Manuf. Polym. Compos. Sci.*, vol. 2, no. 3–4, pp. 117–123, Oct. 2016.

[26] A. Babeau, S. Comas-Cardona, C. Binetruy, and G. Orange, “Modeling of heat transfer and unsaturated flow in woven fiber reinforcements during direct injection-pultrusion process of thermoplastic composites,” *Compos. Part Appl. Sci. Manuf.*, vol. 77, pp. 310–318, Oct. 2015.

[27] R. Arbter *et al.*, “Experimental determination of the permeability of textiles: A benchmark exercise,” *Compos. Part Appl. Sci. Manuf.*, vol. 42, no. 9, pp. 1157–1168, Sep. 2011.

[28] B. Bachmann, D. K. Masania, and C. Dransfeld, “Compression RTM Numerical flw modelling,” FHNW University of Applied Sciences and Arts Northwestern Switzerland, Institute for Polymer Engineering Windisch.

[29] J. Studer, C. Dransfeld, and B. Fiedler, “DIRECT THERMOPLASTIC MELT IMPREGNATION OF CARBON FIBRE FABRICS BY INJECTION MOULDING,” p. 8, 2016.

[30] S. Laurenzi and M. Marchetti, “Advanced Composite Materials by Resin Transfer Molding for Aerospace Applications,” in *Composites and Their Properties*, N. Hu, Ed. InTech, 2012.

[31] P. Rosenberg, R. Chaudhari, M. Karcher, F. Henning, and P. Elsner, “Investigating cavity pressure behavior in high-pressure RTM process variants,” 2014, pp. 463–466.

[32] S. Bickerton, M. J. Buntain, and A. A. Somashekar, “The viscoelastic compression behavior of liquid composite molding preforms,” *Compos. Part Appl. Sci. Manuf.*, vol. 34, no. 5, pp. 431–444, May 2003.

[33] V. I. Osipov, “The Terzaghi Theory of Effective Stress,” in *Physicochemical Theory of Effective Stress in Soils*, Cham: Springer International Publishing, 2015, pp. 35–37.

[34] M. Danzi, “Manufacturing of Polymer Composites OOA Prepreg Technology,” Laboratory of Composite Materials and Adaptive Structures ETH Zürich, Apr-2017.

[35] E. Hajduk, “14.330 SOIL MECHANICS Consolidation,” University of Massachusetts Lowell, MA 01854, USA, Mar-2013.

[36] F. Klunker, M. Danzi, and P. Ermanni, “Fiber deformation as a result of fluid injection: modeling and validation in the case of saturated permeability measurements in through thickness direction,” *J. Compos. Mater.*, vol. 49, no. 9, pp. 1091–1105, Apr. 2015.

[37] “Tegrapol automated polishing machine.” [Online]. Available: http://www.m5universities.ac.uk/facilities/results/view/1675/tegrapol-automated-polishing-machine.html.

[38] “Leno-Woven Non-Crimp Fabrics (NCF).” FTA Forschungsgesellschaft für Textiltechnik Albstadt mbH Parkweg 2 72458 Albstadt, Germany, Jan-2016.

[39] “G3 Digital Cutter, Swiss quality cutting system | ZUND Digital Cutter,” *G3 Digital Cutter, Swiss quality cutting system | ZUND Digital Cutter*, May-2018. [Online]. Available: https://www.zund.com/en/g3-digital-cutter. [Accessed: 27-May-2018].

[40] R. Umer, S. Bickerton, and A. Fernyhough, “The effect of yarn length and diameter on permeability and compaction response of flax fibre mats,” *Compos. Part Appl. Sci. Manuf.*, vol. 42, no. 7, pp. 723–732, Jul. 2011.

[41] “Standard Test Method for Permeability of Granular Soils (Constant Head) ASTM D 2434 – 68,” ASTM International, West Conshohocken, PA, 2006.

APPENDICES

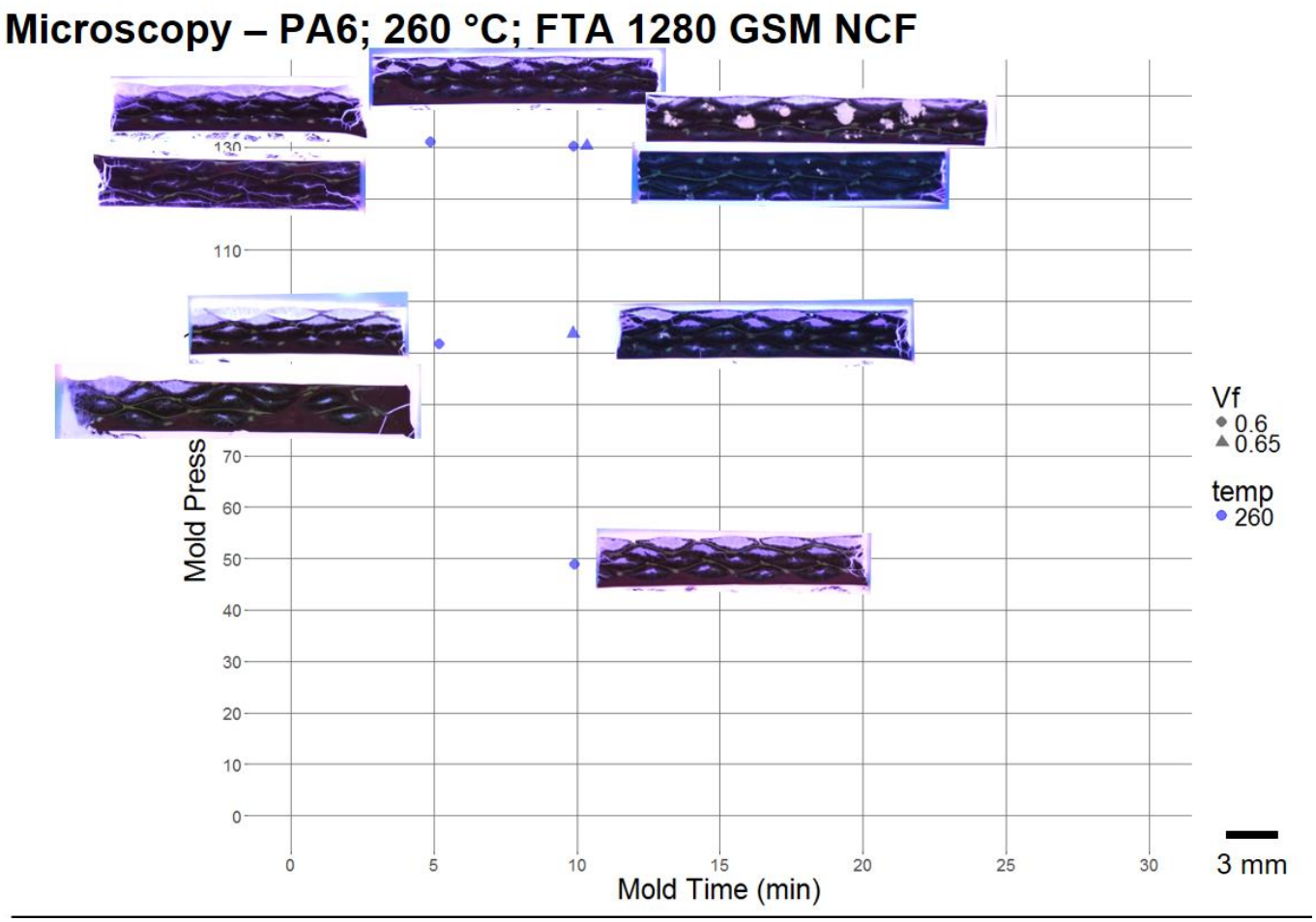
Microscopy – PA6; 260 °C; FTA 1280 GSM NCF
Mold Press
130
110
70
60
50
40
30
20
10
0
0
5
10
15
20
25
30
Mold Time (min)
Vf
0.6
0.65
temp
260
3 mm

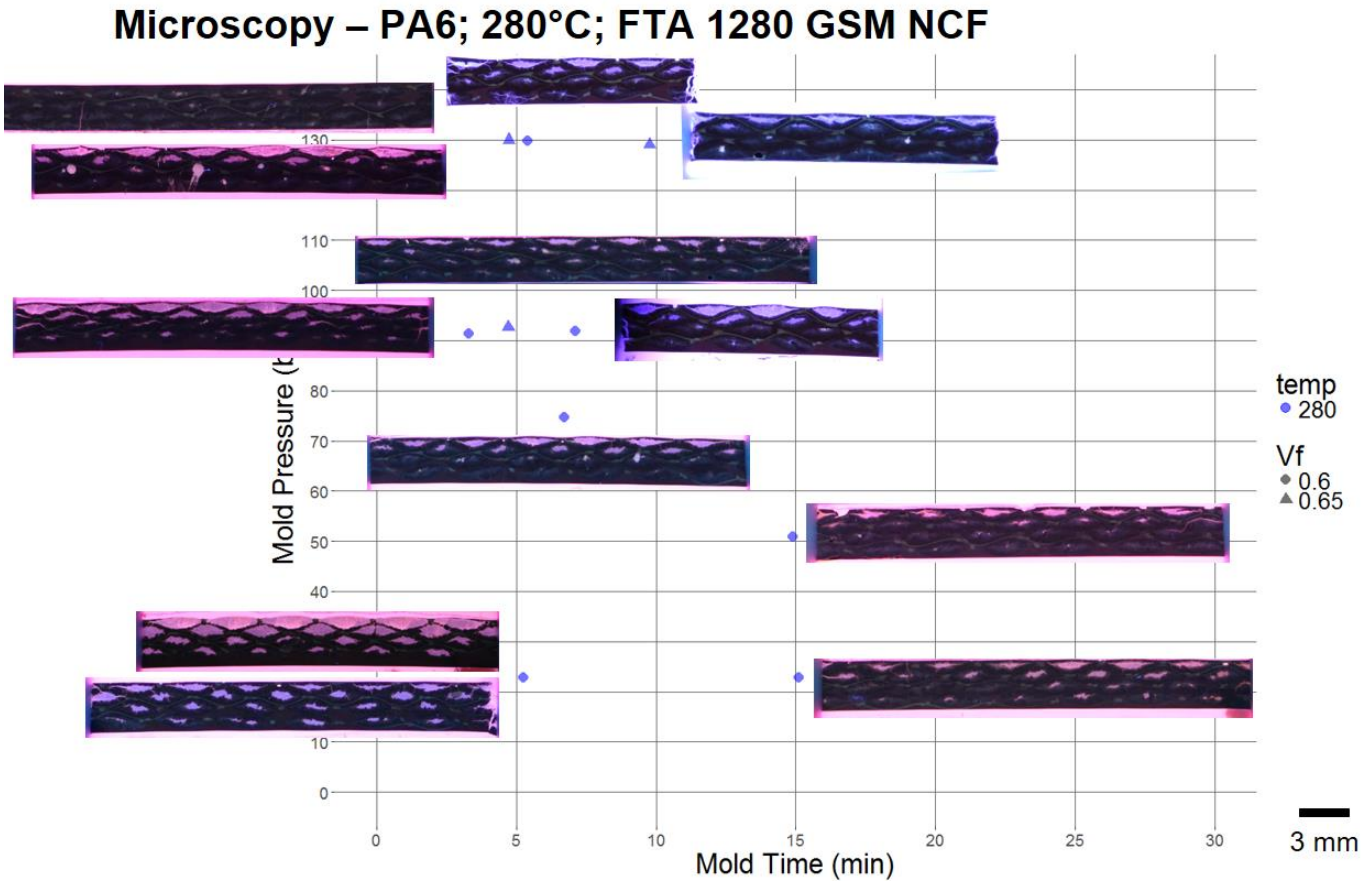
Microscopy – PA6; 280°C; FTA 1280 GSM NCF
Mold Pressure (t
130
110
100
80
70
60
50
40
10
0
0
5
10
15
20
25
30
Mold Time (min)
temp
280
Vf
0.6
0.65
3 mm

Microscopy – PA6; 300 °C; FTA 1280 GSM NCF

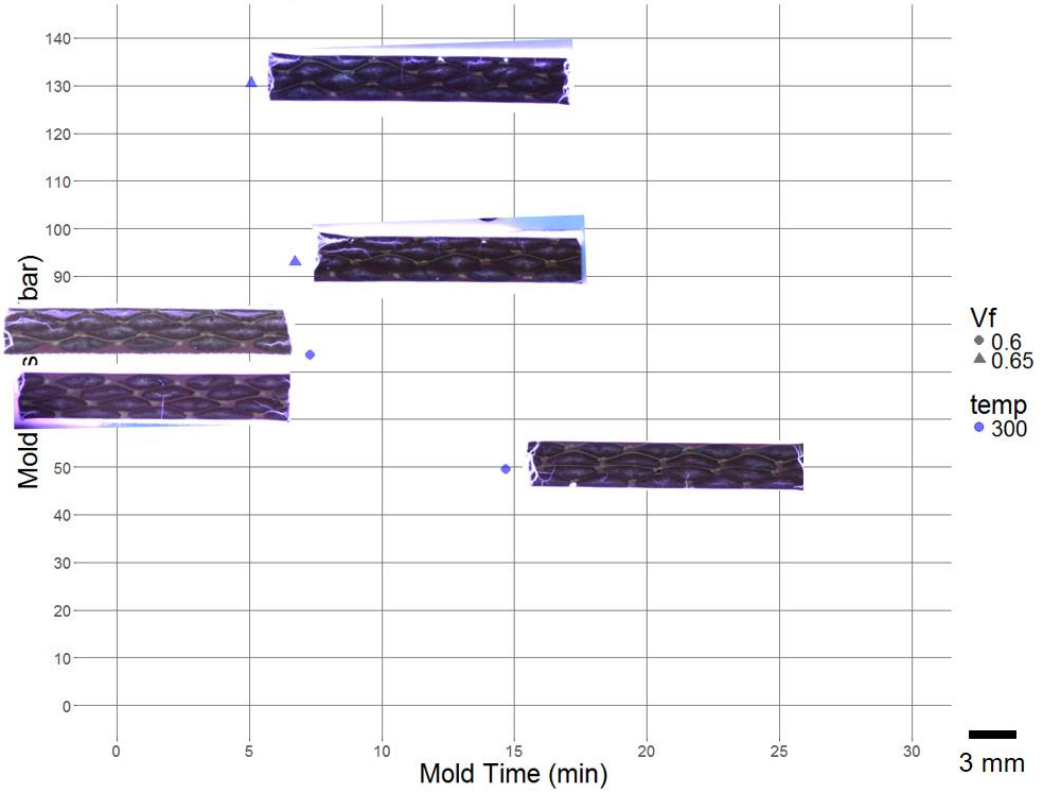

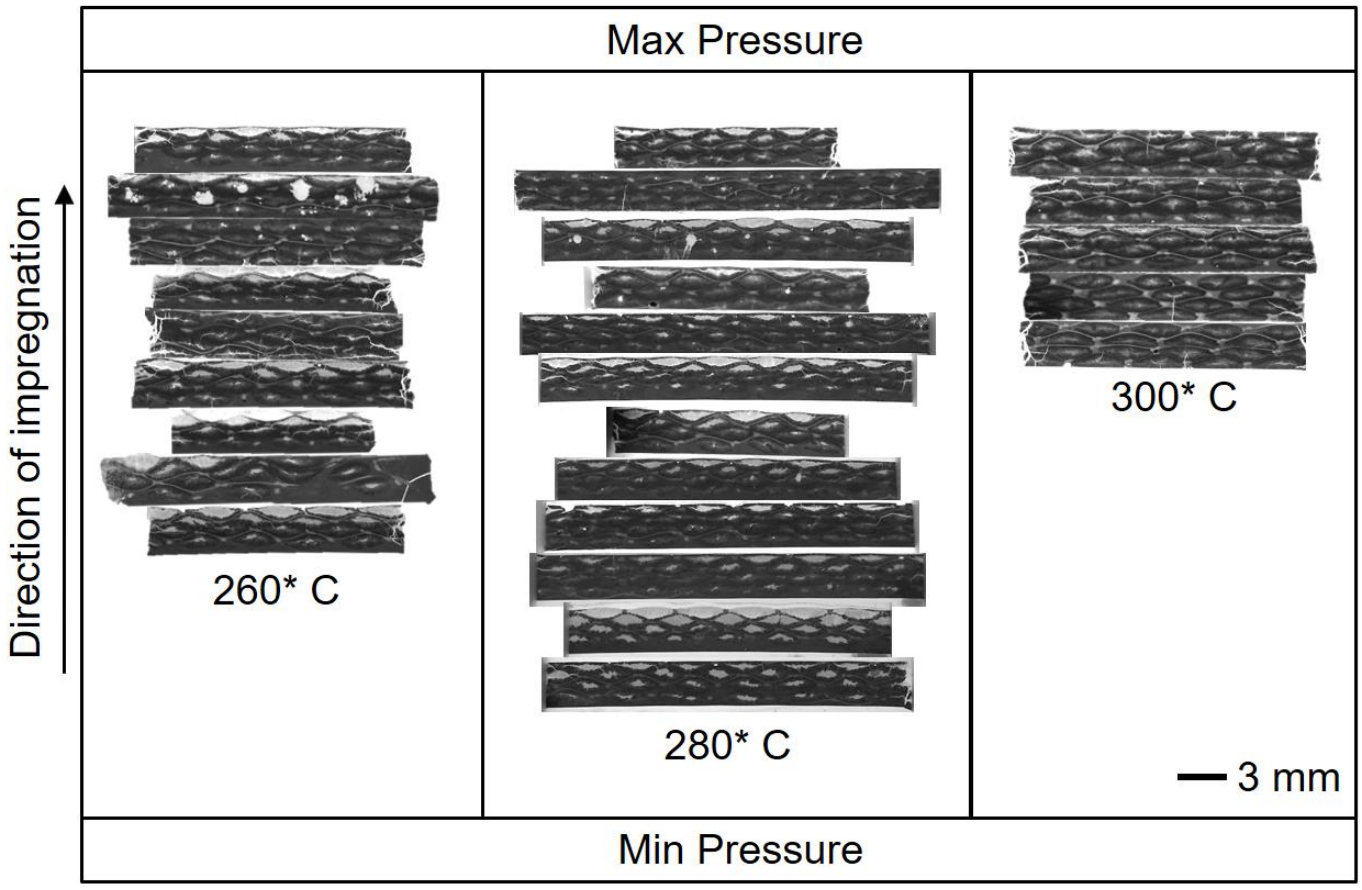
Max Pressure
Direction of impregnation
260* C
280* C
300* C
3 mm
Min Pressure

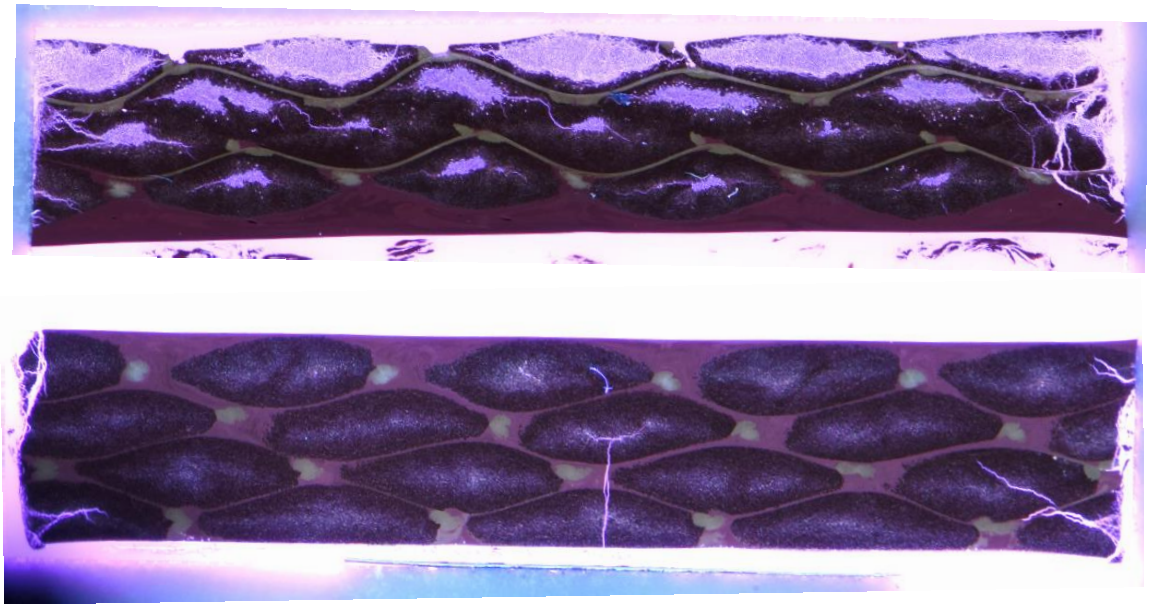

Visible features in UV fluorescent microscopy.